CANCER

Secreted Apoe rewires melanoma cell state vulnerability to ferroptosis

Sanket More[1,2], Julie Bonnereau[1,2], David Wouters[3,4,5], Xander Spotbeen[4,6], Panagiotis Karras[7,8], Francesca Rizzollo[1,2], Theo Killian[8,9], Tom Venken[3,10], Stefan Naulaerts[11], Ellen Vervoort[1,2], Maarten Ganne[1,2], David Nittner[8,12], Jelle Verhoeven[1,2], Oliver Bechter[13], Francesca Bosisio[14], Diether Lambrechts[3,10], Alejandro Sifrim[3,4,5], Brent R. Stockwell[15], Johannes V. Swinnen[6], Jean Christophe Marine[7,8], Patrizia Agostinis[1,2]*

A major therapeutic barrier in melanoma is the coexistence of diverse cellular states marked by distinct metabolic traits. Transitioning from a proliferative to an invasive melanoma phenotype is coupled with increased ferroptosis vulnerability. However, the regulatory circuits controlling ferroptosis susceptibility across melanoma cell states are unknown. In this work, we identified Apolipoprotein E (*APOE*) as the top lipid-metabolism gene segregating the melanoma MITF^{high}/AXL^{low} proliferative/ferroptosis-resistant from MITF^{low}/AXL^{high} invasive/ferroptosis-sensitive state. Mechanistically, ApoE secreted by the MITF^{high}/AXL^{low} cells protects the invasive phenotype from ferroptosis-inducing agents by reducing the content of peroxidation-prone polyunsaturated fatty acids and boosting GPX4 levels both in vitro and in vivo. Whole-exome sequencing indicates that *APOE*^{high} expression in patients with melanoma is associated with resistance to ferroptosis, regardless of *APOE* germline status. In aggregate, we found a ferroptosis-resistance mechanism between melanoma cell states relying on secreted ApoE and *APOE*^{high} expression as a potential biomarker for poor ferroptosis response in melanoma.

INTRODUCTION

The ability of melanoma cells to transition through a spectrum of differentiation states has emerged as a critical barrier to effective and durable therapeutic responses. While the mutational landscape of melanoma has a role in protective mechanisms, recent high-resolution single-cell studies revealed a contribution of nongenetic, adaptive mechanisms to drug resistance (*1*, *2*). By remodeling their transcriptome and chromatin landscape, melanoma cells rapidly adapt to stressful microenvironments and therapeutic pressure (*1*); emerging data highlight the relevance of reprogramming mechanisms related to metabolism, homeostasis, and intercellular communication (*3*–*5*). Key cell-autonomous mechanisms include the maintenance of the cancer cell's redox tone and the remodeling of iron and lipid metabolism. In particular, during multistage cell state transitions, cancer cells acquire a dependency on the ability to detoxify lipid peroxides (*6*). At the same time, the loss of the lipid repair enzyme glutathione peroxidase 4 (GPX4) in invasive cancer cells with a mesenchymal and drug-resistant phenotype causes the accumulation of lipid hydroperoxides (lipid-ROS) triggering the iron-dependent cell death known as ferroptosis (*7*).

Growing evidence indicates that this type of regulated cell death (RCD) represents a cancer cell vulnerability caused by incorporating polyunsaturated fatty acids (PUFAs) into cellular membrane lipids (*8*). While changes in the polyunsaturation of membrane lipids facilitate the invasive and motile cancer phenotype (*9*), cancer cells become susceptible to lipoxygenase/Fenton reaction–induced lipid-ROS damage and are dependent on the activity of GPX4 to maintain viability (*6*).

In melanoma, ferroptosis-inducing agents, such as the system X_c^- inhibitor imidazole ketone erastin (IKE) or (1S, 3R)-RSL3 (RSL3) combined with the BRAF kinase inhibitor vemurafenib, reduced colony formation of invasive melanoma cells in vitro, possibly because of their lower levels of glutathione (*10*). Targeting the dedifferentiated state is thus a viable strategy to overcome melanoma drug resistance and prevent relapse. However, we still lack a comprehensive understanding of how cell-intrinsic metabolic reprogramming affects the vulnerability of drug-resistant/invasive melanoma cells to this form of RCD. Furthermore, our understanding of how the coexistence of (reversible) cellular states within the melanoma ecosystem affects the therapeutic efficacy of ferroptosis-inducing agents is largely incomplete. Given the ability of melanoma cells to promote growth and invasion through the secretion of protumorigenic factors (*11*–*13*), it is plausible that beyond cancer cell–intrinsic mechanisms, phenotype plasticity and ferroptosis vulnerability of drug-resistant clones may involve autocrine or paracrine circuits. Thus, understanding the diversity of the cell-autonomous and non–cell-autonomous mechanisms that melanomas coopt to resist ferroptosis vulnerability is of paramount importance to designing more effective therapeutic strategies targeting drug-resistant clones.

[1]Cell Death Research and Therapy Laboratory, VIB-KU Leuven Center for Cancer Biology, Leuven, Belgium. [2]Department of Cellular and Molecular Medicine, KU Leuven, Leuven, Belgium. [3]Department of Human Genetics, University of Leuven, KU Leuven, Leuven, Belgium. [4]KU Leuven Institute for Single Cell Omics (LISCO), University of Leuven, KU Leuven, Leuven, Belgium. [5]KU Leuven Institute for Artificial Intelligence (Leuven.AI), University of Leuven, KU Leuven, Leuven, Belgium. [6]Laboratory of Lipid Metabolism and Cancer, Department of Oncology, LKI - Leuven Cancer Institute, KU Leuven, 3000 Leuven, Belgium. [7]Laboratory for Molecular Cancer Biology, VIB-KU Leuven Center for Cancer Biology, Leuven, Belgium. [8]Department of Oncology, KU Leuven, 3000 Leuven, Belgium. [9]Laboratory of Neurophysiology in Neurodegenerative Disorders, VIB-KU Leuven, Leuven, Belgium. [10]Translational Genetics Laboratory, VIB-KU Leuven Center for Cancer Biology, Leuven, Belgium. [11]Laboratory of Cell Stress & Immunity, Department of Cellular and Molecular Medicine, KU Leuven, Leuven 3000, Belgium. [12]Spatial Multiomics Expertise Center, VIB-KU Leuven Center for Cancer Biology, 3000 Leuven, Belgium. [13]LKI, Department of General Medical Oncology, Department of Oncology, University Hospitals Leuven, KU Leuven, Leuven, Belgium. [14]Department of Pathology, UZ Leuven, Leuven, Belgium. [15]Department of Biological Sciences and Department of Chemistry, Columbia University, New York, NY 10027, USA.
*Corresponding author. Email: patrizia.agostinis@kuleuven.be

Here, we set out to portray how the rewiring of lipid metabolism and lipid-regulating factors controls cell-autonomous and non–cell-autonomous circuits affecting ferroptosis vulnerability across melanoma states. Using in vitro/in vivo orthogonal approaches and melanoma patient samples, we identified an autocrine ferroptosis-protective mechanism driven by the secretion of the lipoprotein ApoE from the ferroptosis-insensitive melanoma cells. Melanoma-secreted ApoE remodels the redox status and the PUFA-rich lipidome of the ferroptosis-liable/drug-resistant melanoma cells, shielding them from lipid peroxidation–induced cell death in vitro and in vivo.

RESULTS

Lipid remodeling links ferroptosis vulnerability to melanoma cell states

To evaluate whether changes in the membrane lipid composition are causally linked to the differential sensitivity of melanoma cell states to ferroptosis, we analyzed a panel of 12 melanoma cell lines representing cellular models of progressive differentiation. We clustered these cell lines based on the enrichment for specific gene sets and transcription factors into four subtypes. The melanocytic (M) and transitory (T) subtypes expressed a more mature melanocyte signature, marked by high levels of MITF, the master regulator of the differentiation status of melanoma (*14*). The more dedifferentiated neural crest (NC)–like and Undifferentiated (U) subtypes shared low levels of MITF and up-regulation of the receptor tyrosine kinase AXL (Fig. 1A). As expected, irrespective of their mutational status (table S1) or known sensitivity profile toward mitogen-activated protein kinase (MAPK)–targeted agents, most melanoma cells belonging to the U subtype and, to a lesser extent, the NC subtype, succumbed to class-1 (IKE) and class-2 (RSL3) ferroptosis inducers (FINs) (Fig. 1B and fig. S1A). Cell death in the sensitive NC/U subtypes was accompanied by an increase in BODIPY-C11 staining, which was blocked by the radical-trapping antioxidant (RTA) liproxstatin (Lip-1) (Fig. 1C and fig. S1B and C). This cell death was bona fide ferroptosis, as it was inhibited by the iron chelator [deferoxamine (DFO)], the RTA [ferrostatin-1 (Fer-1)], and the inhibitors of lipoxygenases (PD146176 and ML355), but not by the inhibitors of apoptosis (ZVAD-FMK), necroptosis [necrostatin-1s (Nec1s)], cyclooxygenase (Piroxicam), or cytochrome P450 (MSPOOH) (fig. S1D). In contrast, the M and T melanoma cell states showed resistance to cell death (Fig. 1B and fig. S1A).

Three-dimensional (3D) cultures more reliably model cell-cell interactions occurring in vivo and drug-resistance processes, which may affect ferroptosis (*15*). 3D cultures of ferroptosis-resistant M229 cells ($MITF^{high}$, T subtype) stably expressing mCherry were IKE resistant with no detectable signs of lipid peroxidation (Fig. 1, D and E). Conversely, spheroids of ferroptosis-sensitive M229R cells ($MITF^{low}$, U subtype) underwent ferroptosis, accompanied by Lip-1–inhibitable Bodipy C11 staining of lipid peroxides (Fig. 1, D to F), thus phenocopying the responses observed in the 2D culture settings.

The drug-resistant, U cancer cell state displays increased activity of enzymes promoting the synthesis and uptake of PUFAs (*16*, *17*), such as arachidonic acid (AA, C20:4) and linolenic acid (C18:2), which are major substrates for ROS attack. In particular, the oxidation of PUFAs containing phosphatidylethanolamine (PE) molecular species generates ferroptosis signals (*18*). We then subjected melanoma cell lines representative of the four cell states to liquid chromatography–mass spectrometry–based lipidomics. Differentiated melanoma cells exhibited a high content of saturated and monounsaturated fatty acids (S/MUFAs) (Fig. 1G and fig. S1E). Of note, the transition toward the fully U/invasive phenotype was associated with an enrichment in the content of PE, lysophosphatidylethanolamine, and PE-plasmalogens (i.e., vinyl-ether linkage) containing PUFAs (Fig. 1G), and to a lesser extent of PUFA-containing phosphatidylcholines (PCs) (fig. S1E). Consistent with this, principal components analysis (PCA) based on the top 1000 different lipid species across these cell lines clustered M and T cell types with a high content of SFAs/MUFAs from the NC and U melanoma subtypes, which had higher content of PUFA–phospholipids (PLs) (Fig. 1H). In line with previous studies (*18*, *19*), remodeling membrane lipid saturation of melanoma cell types by enriching the membranes of the ferroptosis-resistant melanoma cells with PUFAs (i.e., via supplementation with AA) or those of the ferroptosis-vulnerable cells with MUFAs [i.e., via supplementation of oleic acid (OA)] reverted their susceptibility toward FIN (fig. S1F). Together, these results indicate that the U melanoma cell state is hallmarked by a higher content of PUFAs, especially in PE, which is well-known substrate for lipid peroxidation.

ApoE expression distinguishes melanoma cell states

To identify lipid metabolism gene signatures associated with melanoma cell states, we probed an RNA sequencing (RNA-seq) dataset of 53 human melanoma cell lines subclassified into four subtypes (table S5) (*10*). Unsupervised hierarchical clustering segregated melanoma cell lines into two clusters. Cluster 1 consisted of the M and T subtypes, collectively grouped as proliferative (PRO), and cluster 2 consisted of the NC and U subtypes, together grouped as invasive (INV) (Fig. 2A). Further differential expression (DE) analysis of the top 1200 differential genes identified 186 genes (Fig. 2B). Overrepresentative analysis (ORA) to characterize pathway genes were enriched in identified cholesterol metabolism as the top pathway enriched within the Kyoto Encyclopedia of Genes and Genomes (KEGG) database (Fig. 2C). Apolipoprotein E (*APOE*) was identified as the top DE gene, exhibiting a high expression in PRO [cluster 1 (M, T)] and a low expression in INV [cluster 2 (NC, U)] (fig. S2A) subtypes. A similar pattern of *APOE* expression was apparent in The Cancer Genome Atlas (TCGA) skin cutaneous melanoma (SKCM) bulk tumor expression profiles classified into the four melanoma subtypes (Fig. 2D).

We focused on ApoE since this 34-kDa plasma lipoprotein–binding protein is involved in fatty acid metabolism (*20*) and because tumor-derived ApoE is repressed during melanoma progression (*21*, *22*). Moreover, *APOE* is under transcriptional control of *MITF* (fig. S2E) (*23*), suggesting that this lipoprotein-binding protein may be part of a gene network rewiring lipid metabolism of melanoma states. Consistent with the RNA expression (fig. S2B), ApoE protein levels were high, both intracellularly and as a secreted protein, in $MITF^{high}$ PRO melanoma cells, while it decreased progressively when transitioning from the T to the NC-like cells, to become undetectable in the $MITF^{low}$ INV subtype (Fig. 2, E and F, and fig. S2C). We explored whether *APOE* expression correlated with the emergence of a drug-resistant melanoma phenotype upon exposure to $BRAF^{V600E/k}$ (dabrafenib) and MEK (trametinib) inhibitor treatment. To address this possibility, we performed pseudo-time trajectory analysis using a single-cell RNA-seq data from melanoma patient-derived xenografts (PDX),

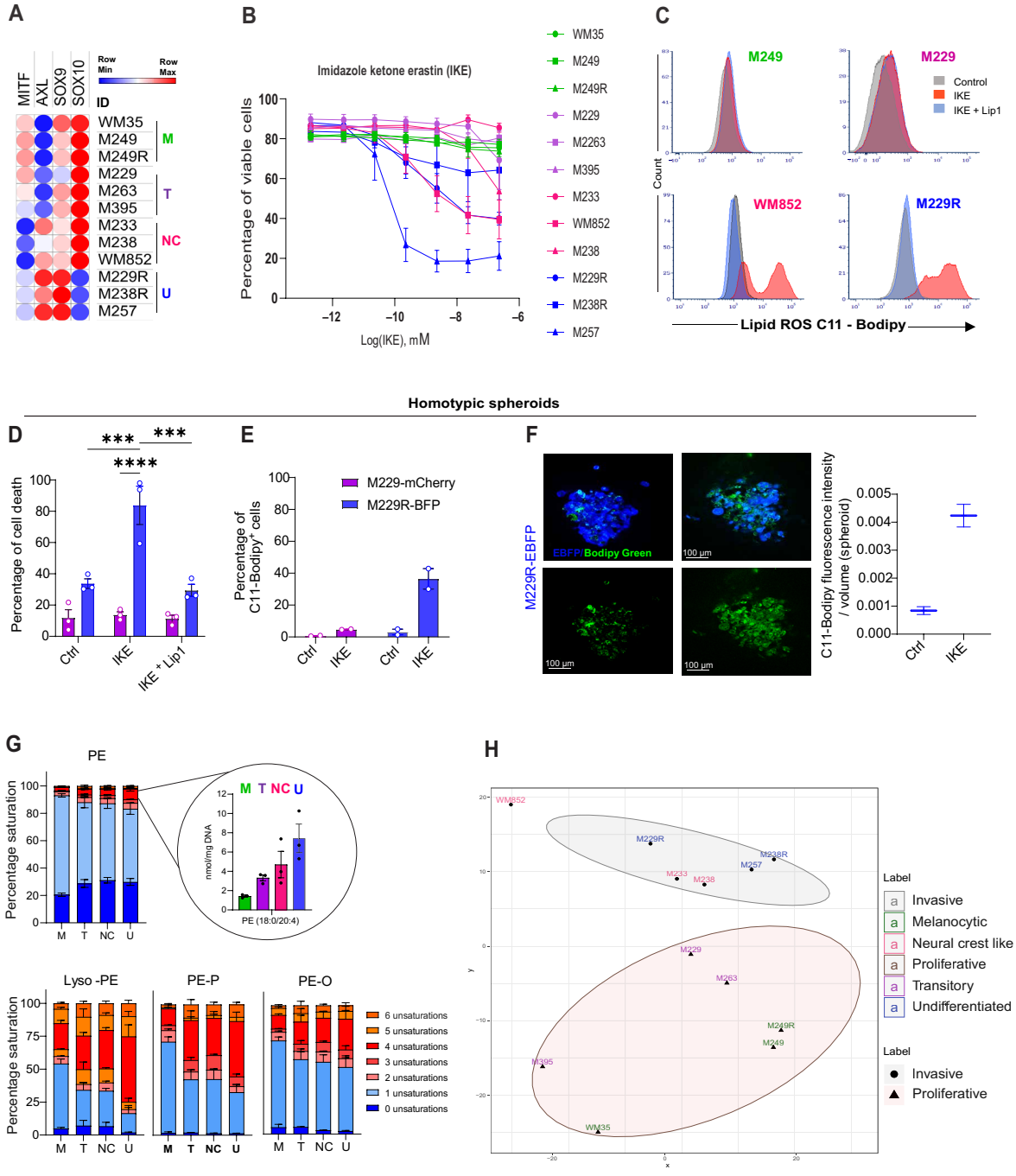

Fig. 1. Lipid remodeling links ferroptosis vulnerability to melanoma cell states. (**A**) Heatmap showing expression of melanoma subtype-specific marker genes analyzed by quantitative polymerase chain reaction (qPCR) in different melanoma cell lines ($n = 1$ with three technical replicates, 2^ΔCT values were $\log_2$ transformed). (**B**) Dose curve response showing sensitivity of subtype-specific melanoma cell lines toward IKE. Cells were treated with indicated concentration of IKE for 24 hours, and cell death was analyzed using Sytox-green assay ($n = 3$). (**C**) Representative histograms from fluorescence-activated cell sorting (FACS) analysis showing lipid-ROS induction analyzed by Bodipy C11 assay across different melanoma cell lines after treatment with IKE (1.25 µM, 16 hours). Lip1 (1 µM) was used as a ferroptosis inhibitor. (**D**) Bar plot showing the effect on the sensitivity of M229-mCherry (T) and M229R-EBPF (U) cells toward IKE (10 µM, 24 hours) when cultured in 3D spheroids. Lip1 (2 µM) was used as a ferroptosis inhibitor. Cell death was analyzed using eFluor 780 viability dye [$n = 3$, two-way analysis of variance (ANOVA) with Tukey's multiple comparison test]. (**E**) Bar plot showing the percentage of lipid peroxidation analyzed by Bodipy C11 assay in homotypic spheroids of M229-mCherry and M229R-EBFP cells ($n = 2$). (**F**) (Right) Representative image of spheroids of M229R-EBFP cells showing Bodipy C11 fluorescence intensity upon treatment with IKE (10 µM, 2 hours). (Left) Bar plot showing total Bodipy C11 fluorescence intensity measurement in spheroid upon treatment with IKE (10 µM, 2 hours) ($n = 2$). (**G**) Stack bar plot showing the percentage of saturation in different subclasses of PE species across different melanoma subtypes. Zoom image indicating quantitative level of PE-AA aross different melanoma subtypes (values represent the mean of three different cell lines across each subtype). (**H**) PCA plot showing clustering pattern of melanoma cell lines based on the top 1000 lipid species different across cell lines (quantitative data was $\log_2$ transformed). All data represent means ± SEM. *$P < 0.05$, **$P < 0.01$, ***$P < 0.01$, ****$P < 0.0001$.

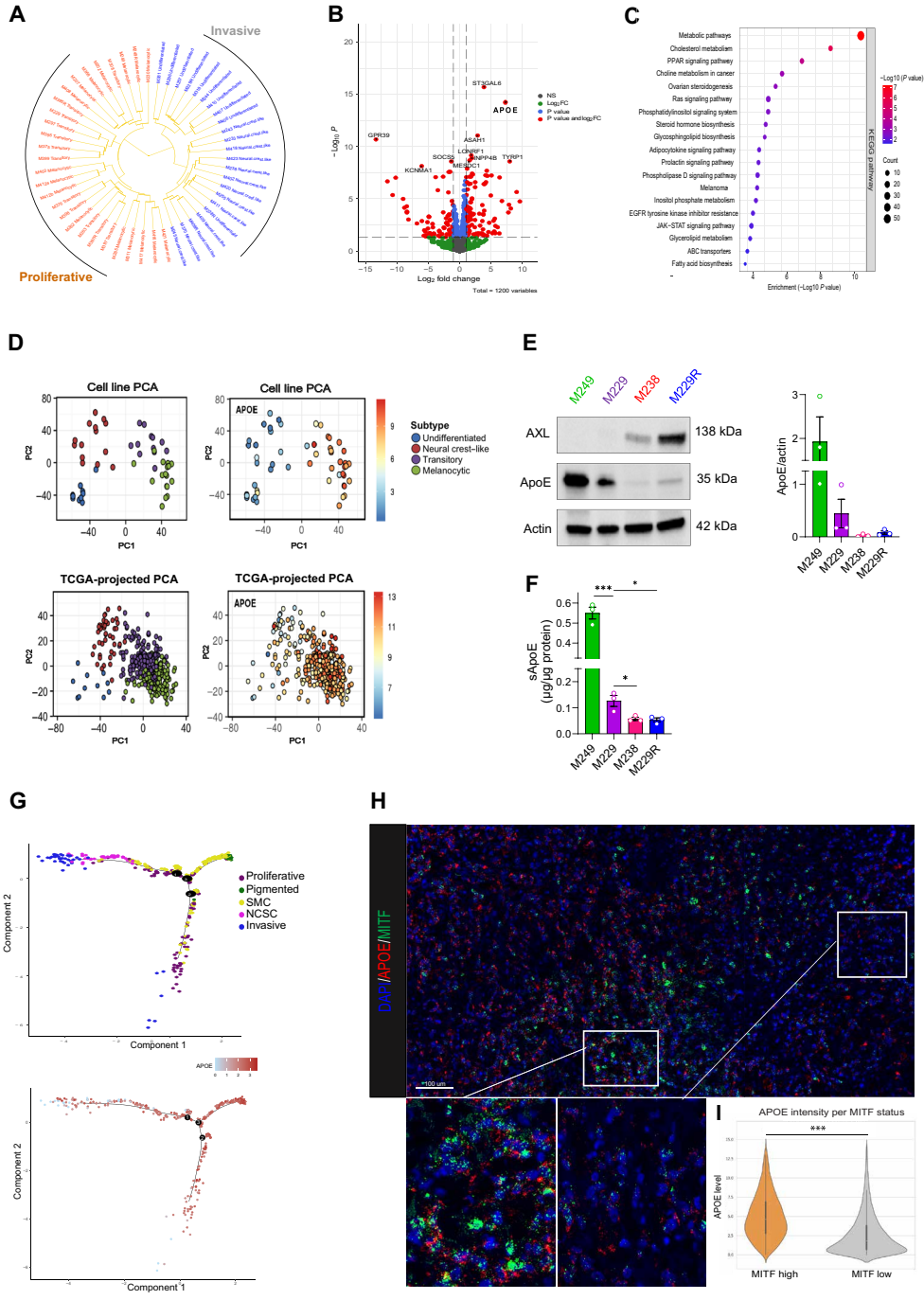

Fig. 2. ApoE expression distinguishes melanoma cell states. (**A**) Circular phylogenetic tree showing clustering of melanoma cell lines based on genes involved in lipid metabolism. (**B**) Volcano plot showing DEGs between proliferative and invasive subtypes of melanoma cell lines (DE analysis was performed on top 1200 genes from lipid metabolism meta-list different across proliferative and invasive subtypes of melanoma cell lines, genes with $\log_2$ fold change >1 and adjusted *P* value <0.05 were considered as differentially expressed). (**C**) Bubble plot showing pathways enriched after ORA on DEGs (size of the bubble represents the count of genes contributing to the pathway and color represents $-\log_{10}$ *P* value (adjusted *P* value) indicating statistical significance of enrichment). (**D**) PCA plots showing expression of *APOE* in bulk RNA-seq dataset from melanoma cell lines and patient-derived bulk tumor (SKCM-TCGA dataset) stratified across different subtypes of melanoma. (**E**) Representative Western blot with corresponding bar plot showing quantification of intracellular protein level of ApoE across different subtypes of melanoma cell lines ($n = 3$). (**F**) Bar plot showing the secreted level of ApoE/microgram of protein across different melanoma subtypes ($n = 3$, unpaired Student's *t* test calculated separately for comparison of two sets of data points). (**G**) scRNA-seq analysis to monitor the expression of *APOE* across the developmental trajectory of melanoma cells in response to the drug. Top, monocle-based pseudo-time ordering to build the trajectory of drug-exposed melanoma cells. Bottom, expression of *APOE* across the trajectory of melanoma cells. (**H**) Representative confocal image showing mRNA expression of the *MITF* and *APOE* genes, as detected by RNAscope, in melanoma patient–derived tumor section. Zoomed images show area with *MITF*^{High} *APOE*^{High} cells (left) and *MITF*^{Low} *APOE*^{Low} cells (right). (**I**) Violin plot showing expression of *APOE* in *MITF*^{High} and *MITF*^{Low} melanoma cells (unpaired Student's *t* test).

portraying the dynamics of melanoma cell-state transition in response to therapeutic pressure (*1*). *APOE* was highly expressed in the PRO melanoma lineages, while being down-regulated over time in the drug-resistant NC-like and INV melanoma states, with more metastatic potential (Fig. 2G and fig. S2D).

We validated these findings in drug-naive metastatic melanoma biopsies by visualizing the spatial expression of *APOE* within the main $MITF^{high}$ (PRO) or $MITF^{low}$ (INV) melanoma phenotypes, using RNA in situ hybridization (RNAscope). Consistent with what we observed in melanoma cell lines and the PDX model, the major population of $MITF^{high}$ PRO melanoma cells had high *APOE* expression, while the $MITF^{low}$ INV cell population harbored significantly lower *APOE* levels (Fig. 2, H and I). We conclude that the change in the expression of ApoE is a trait of melanoma cell state transition.

Secreted ApoE shields melanoma cells from the propagation of ferroptosis signals

To test the correlation between melanoma cell expression of *APOE* and response to FINs, we mined the drug sensitivity profiles available from the pharmacogenomics database Cancer Therapeutics Response Portal (CTRP). The INV cells displayed an increased sensitivity toward FINs compared with PRO cells (fig. S3A). Notably, *APOE* expression correlated with resistance to the class-2 FINs, RSL3, ML210, and ML162, and showed a similar trend for the class-1 FIN, Erastin (Fig. 3A and fig. S3B).

Next, we explored these data at the protein/signaling levels. Because to perform its function, ApoE must be secreted and lipidated (*24*); thus, we tested whether secreted (s)ApoE exerted a protective effect in the ferroptosis-vulnerable INV melanoma cells. INV cells exposed to conditioned media from the ferroptosis-insensitive PRO cells became resistant to the lethal effects of FINs. This protection was sApoE dependent since the addition of an ApoE-neutralizing antibody (ID7) to the conditioned media reversed this effect (Fig. 3B and fig. S3C).

We then cocultured the isogenic pair of PRO M299-mCherry and INV M229R-EBFP cells at a ratio of 40:60% due to the higher proliferative capacity of the PRO cells, with or without the addition of the ApoE-neutralizing antibody 1D7 for 24 hours, followed by treatment with IKE (Fig. 3C). Compared with the induction of ferroptosis observed in the INV M229R-EBFP cells when cultured alone (80%), the extent of ferroptosis significantly dropped (30 to 40%) in coculture with the PRO M229-mCherry cells (Fig. 3D). In the presence of the ApoE-neutralizing antibody (1D7), IKE-mediated ferroptosis was significantly restored to levels (70%) comparable to those observed in the ferroptosis-sensitive M229R cells (Fig. 3D). Neutralizing ApoE had no effect in the ferroptosis-insensitive cells when cultured alone (fig. S3D).

We evaluated IKE-mediated cell death in heterotypic spheroids formed by mixing M229R-EBFP and M229-mCherry cells in a 40:60 ratio. These spheroids are organized in a central region formed mainly by the PRO M229-mCherry cells surrounded by the ferroptosis-sensitive M229R-EBFP cells, with each cell type making up ~50% of the spheroid after 3 days of coincubation (Fig. 3, E to G). We exposed these 3D cultures to IKE and used Lip-1 to validate the induction of ferroptosis (Fig. 3H). Consistent with the 2D coculture results (Fig. 3D), M229R-EBFP cells contributed more toward the IKE-induced cell death when compared with untreated conditions (Fig. 3H). Analyzing the kinetics of cell death, we observed that the heterotypic spheroid showed a reduced basal and IKE-induced cell death when compared with the highly sensitive M229R-EBFP homotypic spheroid (Fig. 3I). This protective effect was contact independent as conditioned media from the M229-mCherry homotypic spheroid inhibited ferroptosis in the M229R-EBFP cells (Fig. 3J). Hence, secretion of ApoE by PRO cells can attenuate ferroptosis in INV cells in a contact-independent manner, thus portraying sApoE as a lipid-ROS–protective autocrine signal in melanoma.

Blockade of ferroptosis in invasive melanoma cells requires ApoE receptor and lipid-binding domains

Structurally, ApoE has two main domains that are connected by a hinge region (amino acids ~165 to 215); the N-terminal domain (amino acids 1 to 191) forms the receptor binding region, and the C-terminal domain (amino acids ~225 to 299) harbors the major lipid-binding region (amino acids ~244 to 272) (Fig. 4, A and C) (*20*). The binding of lipids is required for ApoE to acquire a biologically active conformation, which is necessary for recognition and binding to the members of the low-density lipoprotein receptor (LDLR) family and its internalization (*24*).

To gain more insights into the structural/lipid-binding function of the ApoE variants and their relevance in mitigating the ferroptosis of highly sensitive melanoma cells, we exposed INV M229R cells to similar concentrations of recombinant human (rh) ApoE2, ApoE3, or ApoE4, before inducing FIN-mediated cell death. All three rhApoE variants were able to rescue ferroptosis induced by IKE or RSL3 (Fig. 4B). Of note, under the same experimental settings, rhApoE failed to protect INV cells against cell death induced by H_2O_2 (fig. S4, C and D), further suggesting that its mitigating action is pronouncedly directed toward lipid peroxides rather than a general prooxidant stress.

Next, we truncated ApoE3, the higher allelic frequency isoform (mean global frequency ~78%) (*20*), at the receptor binding (N-terminal) or the lipid binding (C-terminal) domains. Compared with full-length rhApoE3, the removal of either the N-terminal receptor binding domain or the C-terminal domain of ApoE3 generated ApoE variants (Fig. 4C) that lost the ability to attenuate ferroptosis (Fig. 4D and fig. S4A) in the susceptible INV cells. Furthermore, when these cells were cultured in lipoprotein-deficient media, full-length rhApoE3 failed to protect them from the induction of ferroptosis (Fig. 4E and fig. S4B).

Silencing ApoE expression in PRO cells did not sensitize them to FINs (Fig. 4G and fig. S4E) and did not affect their S/MUFAs-enriched lipid profile (fig. S4G). This suggests that the intracellular loss of ApoE is per se insufficient to remodel the lipid metabolic features that support resistance to FINs in PRO melanoma cells. It is also possible that loss of ApoE may be compensated by the up-regulation of other apolipoproteins. In line with this hypothesis, silencing *APOE* expression in PRO cells caused the up-regulation of *APOA2*, a common protein constituent of the high-density lipoprotein as ApoE, with shared function in lipid metabolism and cholesterol pathway/transport (fig. S4F) (*25*). Together, these results indicate that both the receptor binding and lipid-binding domains of ApoE are functionally required for its ferroptosis-protective effects in INV melanoma cells (Fig. 4F).

ApoE blunts ferroptosis by inducing early lipid remodeling followed by GPX4 elevation in an isoform-independent manner

ApoE is a multifunctional protein with allele-specific antioxidant properties and the capability to regulate lipid metabolism. We first assessed whether sApoE anti-ferroptosis action involved changes

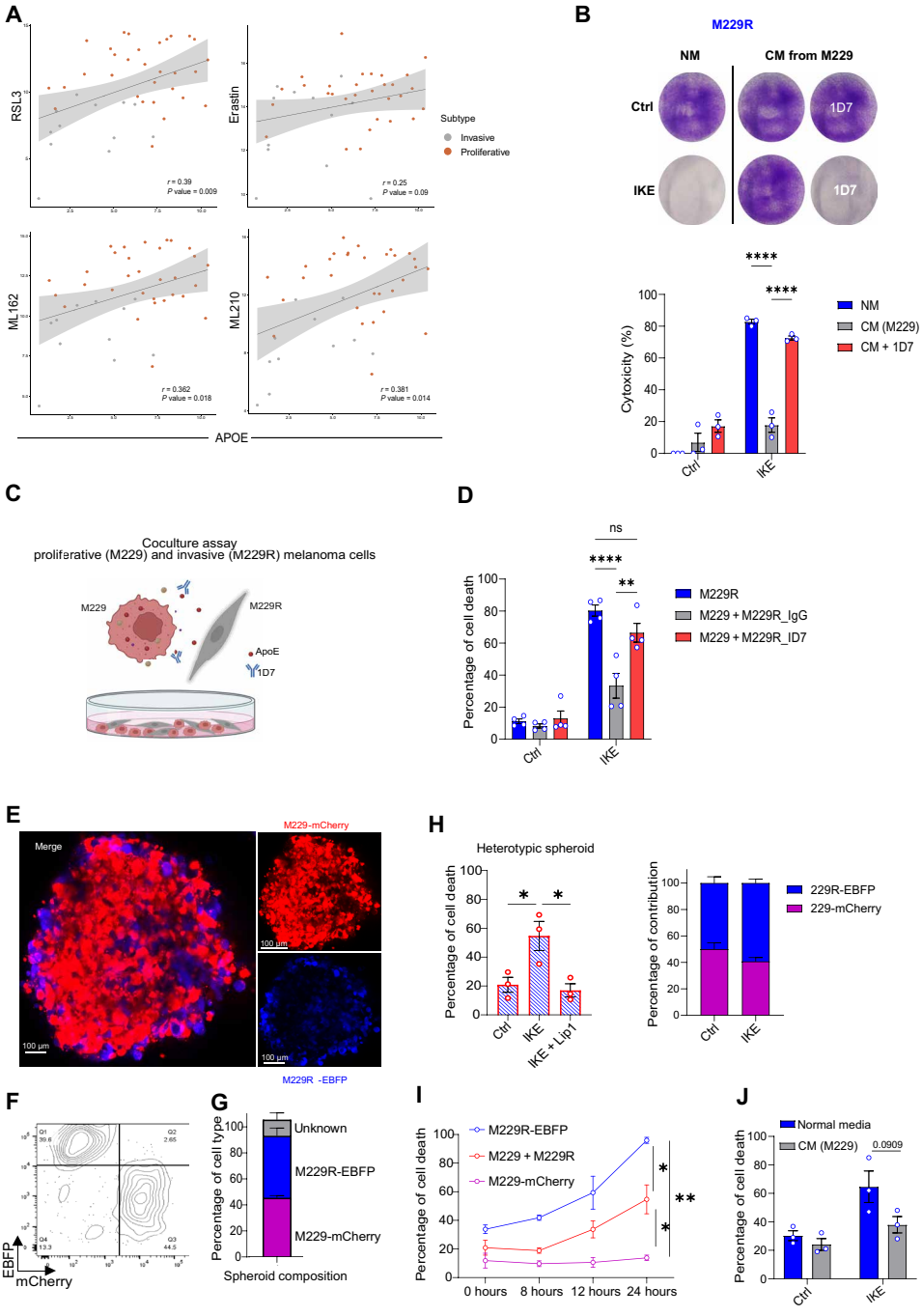

Fig. 3. Secreted ApoE shields melanoma cells from the propagation of ferroptosis signals. (**A**) Scatter plot showing correlation between expression of *APOE* and FINs AUC values from the CTRP database. (**B**) Crystal violet assay and cytotoxicity analysis of M229R cells treated with IKE (1.25 μM, 24 hours) after 3-day incubation with CM from M229 cells, with isotype control or ApoE-neutralizing antibody (1D7, 30 μg/ml) ($n = 3$, two-way ANOVA with Tukey's multiple comparison. NM, normal media; CM, conditioned media). (**C**) Schema showing experimental setup for coculture assay (created with BioRender.com). (**D**) Bar plot showing the effect on sensitivity of M229R-EBFP cells toward IKE (1.25 μM, 24 hours) when in coculture with M229-mCherry cells, with isotype control or ApoE-neutralizing antibody (1D7, 10 μg/ml) ($n = 4$, two-way ANOVA with Tukey's multiple comparison). (**E**) Representative figure showing the organization of M229-mCherry and M229R-EBFP cells in heterotypic spheroid. (**F** and **G**) Representative contour plot from FACS analysis and Stack bar plot showing the percentage of each cell type in the spheroid. (**H**) Bar plot showing the effect on the sensitivity of heterotypic spheroid toward IKE (10 μM, 24 hours) ($n = 3$, one-way ANOVA with Tukey's multiple comparison). Stack bar plot the showing percentage of contribution by each cell type toward cell death in heterotypic spheroid. (**I**) Dot plot showing the effect on the sensitivity of M229-mCherry and M229R-EBFP cells toward IKE (10 μM) in homotypic spheroid and when in c-culture as heterotypic spheroid across different time points ($n = 3$, one-way ANOVA with Tukey's multiple comparison calculated for end time point). (**J**) Bar plot showing the effect on the sensitivity of M229R-EBFP cells toward IKE (10 μM, 24 hours) in homotypic spheroid after 24 hours of incubation with CM from M229-mCherry cells in homotypic spheroid. ($n = 3$, two-way ANOVA with Tukey's multiple comparison). Cell death analyzed using viability dye eFluor780. All data represent means ± SEM. $^*P < 0.05$, $^{**}P < 0.01$, $^{***}P < 0.01$, $^{****}P < 0.0001$. ns, not significant.

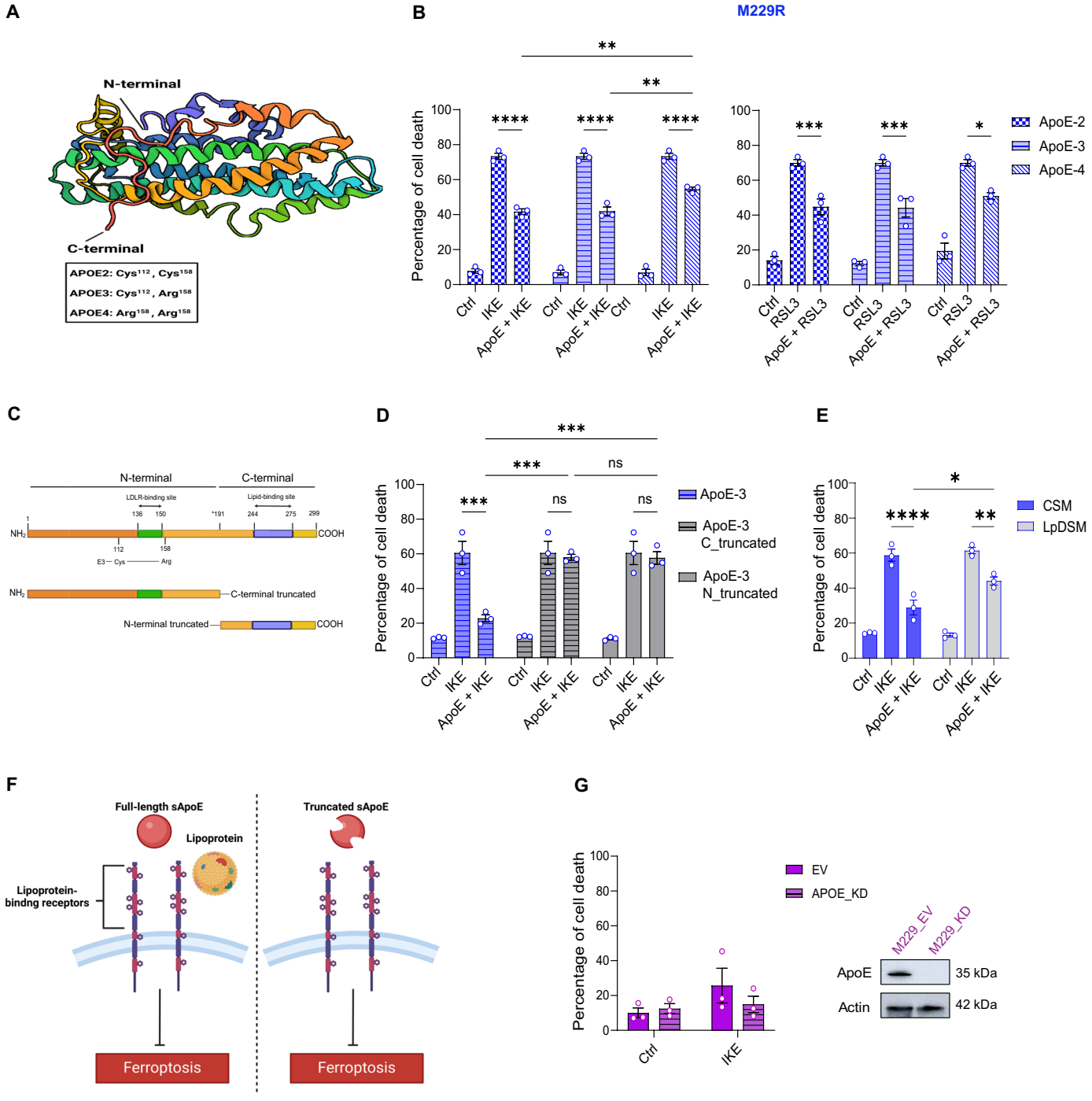

Fig. 4. Blockade of ferroptosis in invasive melanoma cells requires ApoE receptor binding and lipid-binding domains. (**A**) Schematic representation for 3D protein structure of ApoE [based on the structure by Chen *et al.*, (*71*), cartoon version created with BioRender.com]. (**B**) Bar plot showing the effect on the sensitivity of M229R cells toward IKE (1.25 μM, 24 hours) or RSL3 (0.5 μM, 24 hours) after 3 days of treatment with different isoforms of rhApoE (200 μM). Cell death was analyzed using Sytox-green assay ($n = 3$, two-way ANOVA with Tukey's multiple comparison test). (**C**) Schematic representation for protein domains of ApoE (created with BioRender.com). (**D**) Bar plot showing the effect on the sensitivity of M229R cells toward IKE (1.25 μM, 24 hours) after 3 days of treatment with either active or C/N-terminal truncated rhApoE3 (200 μM). Cell death was analyzed using Sytox-green assay ($n = 3$, two-way ANOVA with Tukey's multiple comparison test). (**E**) Bar plot showing the effect on the sensitivity of M229R cells toward IKE (1.25 μM, 24 hours) after 3 days of treatment with rhApoE3 (200 μM), with or without lipoprotein in the media. Cell death was analyzed using Sytox-green assay ($n = 3$, two-way ANOVA with Tukey's multiple comparison test). (**F**) Schematic representation showing the effect of truncation of the ApoE protein or loss of lipoprotein on ferroptosis regulation potential of ApoE (created with BioRender.com). (**G**) (Left) Bar plots showing the effect on the sensitivity of M229 cells toward IKE (1.25 μM, 24 hours) following shRNA-mediated knockdown (KD) of *APOE* compared to empty vector (EV) control ($n = 3$). (Right) Representative Western blot showing knockdown (KD) level of ApoE protein in M229 cells. All data represent means ± SEM. $^*P < 0.05$, $^{**}P < 0.01$, $^{***}P < 0.01$, $^{****}P < 0.0001$.

in the lipidome of the INV melanoma cells and specifically their PUFA's content. Comparing the lipid profiles of untreated and rhApoE3-conditioned INV cells did not reveal changes in the saturation status of PLs (fig. S5A). However, following the treatments with rhApoE3, we observed a reduction in the total content of Lyso-PLs containing PUFAs (Fig. 5A), which are one of the main lipid species found enriched in melanoma cells transitioning toward the U cell state (Fig. 1G).

Lyso-PLs are mainly synthesized by the enzymatic activity of phospholipases (*26*), of which three major classes differing in the catalytic activity are known: PLA (consisting of A1 and A2), PLC, and PLD. PLA1 and PLA2 target the sn-1 and sn-2 positions of PLs, respectively, and hydrolyze the ester bond, releasing free fatty acids and Lyso-PLs (*26*). We reasoned that, because of its ability to hydrolyze PLs, including PC, PS, and PA, into AA (*26*), PLA2 could be a potential target of the anti-ferroptosis activity of sApoE. PLA2 consists of four major types, secretory PLA2 (sPLA2), cytosolic Ca^{2+}-dependent PLA2 (cPLA2) and Ca^{2+}-independent PLA2 (iPLA2), and lipoprotein-associated PLA2 (lpPLA2) (*27*). Each type of PLA2 has a substrate-specific activity, and depending on the substrate, PLA2 can either promote or block ferroptosis (*28*–*31*).

To examine whether a specific PLA2 isoform could be involved in the anti-ferroptosis effect mediated by sApoE in melanoma cells, we tested chemical inhibitors of different isoforms of PLA2. The cPLA2 blocker arachidonyl trifluoromethyl ketone (ATK) protected the susceptible INV cells in a dose-dependent manner from IKE-induced ferroptosis. By contrast, inhibitors of the secretory (varespladib) or lipoprotein-associated (darapladib) PLA2 used within a concentration range that was not cytotoxic per se (*32*, *33*), failed to do so (fig. S5, B to D). cPLA2 catalyzes the hydrolysis of PLs, generating Lyso-PLs and AA (*34*). Release of AA from the sn-2 position of PLs by cPLA2 enables its lipoxygenase-catalyzed peroxidation (*35*). In line with the lipidomics data indicating a specific reduction in Lyso-PLs rather than a broader effect on PUFA levels, rhApoE3 reduced the enzymatic activity of cPLA2 in INV cells (fig. S5E). Of note, measurements of Ca^{2+} levels in INV cells showed that rhApoE3 reduced intracellular calcium levels (fig. S5P), in line with previous data (*36*). Since variation in nanomolar concentrations of intracellular Ca^{2+} impairs cPLA2 translocation to the cellular membrane and its subsequent activation (*37*), this observation suggests a calcium-mediated mechanism for the reduced cPLA2-mediated synthesis of Lyso-PLs containing PUFAs in INV cells.

We then investigated whether restoring the cellular availability of the enzymatic product of cPLA2 by the exogenous addition of a PUFA Lyso-PL (arachidonoyl lysophosphatidic acid/Lyso-AA) could resensitize ApoE-inhibited INV melanoma cells to FINs. Supplementing the PUFA Lyso-PL (Lyso-AA) to the conditioned media from PRO cells or directly to the rhApoE-treated melanoma cells restored their sensitivity to FINs (Fig. 5, B and D, and fig. S5, H and L). Similar effects were observed with the chemical inhibitor of cPLA2 (fig. S5, F and J). By contrast, the MUFA Lyso-PL (1-oleoyl lysophosphatidic acid/Lyso-OA) failed to sensitize ApoE-treated INV cells to ferroptosis (Fig. 5, C and E, and fig. S5, G, I, K, and M).

ApoE is known to import selenoprotein P (SELENOP), a major selenium (Se)–containing protein in plasma that is required for the synthesis of selenoenzymes such as GPX4 (*38*, *39*). We then asked whether sApoE in INV melanoma cells could influence the protein expression of the major antioxidant enzyme GPX4. Extending the exposure of INV melanoma cells to rhApoE for 6 days resulted in elevated GPX4 protein expression. GPX4 protein levels were notably triggered by all three ApoE isoforms (Fig. 5, F and G, and fig. S5R). This increase in GPX4 was also associated with a reduction in the levels of the INV marker AXL, while changes in the key melanocytic marker MITF were not consistently observed (Fig. 5, F to H, and fig. S5R). To generalize this observation, we exposed INV M238R cells to the ApoE-rich conditioned media from M229 PRO cells and evaluated the changes in protein levels of these markers. Also in INV M238R cells, we observed a similar trend, a reduction in the protein levels of AXL accompanied by an increase in the expression of GPX4 after the treatment with the ApoE-rich conditioned media from the M229 cells (fig. S5Q). This suggests the ability of sApoE to mitigate the invasive phenotype of melanoma cells while concomitantly reversing its ferroptosis-vulnerable status. Intriguingly, along with the enhanced expression of GPX4 (Fig. 5, F to H, and fig. S5R), all ApoE isoforms also caused the accumulation of the nuclear factor erythroid 2–related factor 2 (NRF2), the key regulator of components of the antioxidant and detoxification systems (*40*), and increased the expression of known target genes of this transcription factor including *SLC7A11*, *AKR1C1*, and *FTH1* (fig. S5S) (*41*–*45*). Together, these data highlight that sApoE blunts ferroptosis in INV melanoma by the activation of multiple effector mechanisms, involving an initial remodeling of AA metabolism followed by a progressive increase in GPX4 and a more general NRF2 antioxidant program.

Melanoma-associated sApoe increases resistance to ferroptosis in vivo

To examine whether ApoE reduces the therapeutic induction of ferroptosis in melanoma in vivo, we used a transplantable murine melanoma model as xenografts of subcutaneously implanted human M229, and M229R cells failed to grow proficiently. Since small-molecule GPX4 inhibitors are known for their poor bioavailability, we use IKE as in vivo ferroptosis agent. We first tested the in vitro sensitivity of a panel of murine melanoma cell lines, including the Yumm 1.7, Yumm 2.1, and Yumm 3.3 cell lines toward FINs. All these murine melanoma cell lines were *Sox10* positive and expressed very low levels of *Apoe* and *Mitf* (fig. S6A). These murine melanoma cell lines readily succumbed to lethal concentrations of both IKE and RSL3 (Fig. 6A and fig. S6B) through a selective Fer-1 and DFO-inhibitable ferroptosis (fig. S6C). Next, we conditioned these murine cell lines with rhApoE3 and tested their sensitivity toward IKE. When compared with their respective untreated cells, rhApoE3 blunted IKE-mediated cell death in all murine cell lines, although the protective effect was more pronounced in the Yumm 3.3 cells (Fig. 6B).

We subcutaneously injected untreated or rhApoE3-treated Yumm 3.3 cells in $Apoe^{-/-}$ C57BL/6 gender-matched (female) mice to rule out the participation of stroma-derived Apoe. Once the tumors reached a volume of 100 mm^3, the mice were treated with daily intraperitoneal injections of vehicle, IKE (40 mg/kg), or IKE plus Lip-1 (20 mg/kg) for 10 days (Fig. 6C). Melanoma growth was similar in untreated or rhApoE3-treated Yumm 3.3 cells (Fig. 6D), indicating that exposure to rhApoE3 does not confer a growth advantage to these murine melanoma cells in vivo. Administration of IKE reduced but did not abrogate tumor burden when compared with vehicle-treated mice (Fig. 6D). The tumor burden control mediated by IKE was accompanied by a decrease in tumor weight (fig. S6D). However, IKE antitumor effects were countered by the RTA Lip-1, suggesting

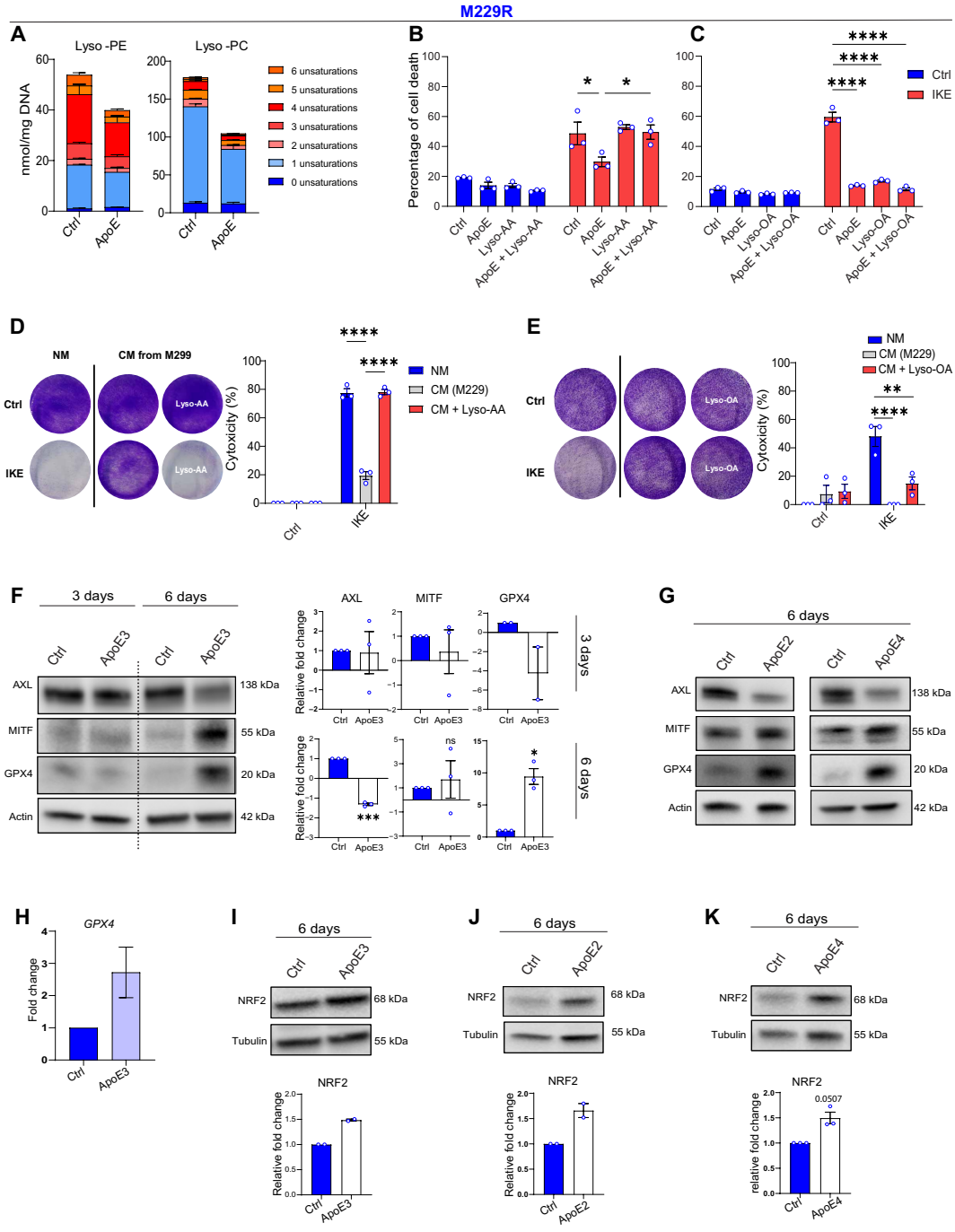

Fig. 5. ApoE blunts ferroptosis by inducing early lipid remodeling followed by GPX4 elevation in an isoform-independent manner. (**A**) Stack bar plot showing the quantity of Lysophospholipid species together with the percentage of saturation in M229R cells treated or untreated with rhApoE3 (200 μM) for 3 days ($n = 3$). (**B** and **C**) Bar plot showing the effect on the sensitivity of M229R cells toward IKE (1.25 μM, 24 hours) after 3 days of treatment with rhApoE2 (200 μM), with or without Lyso-AA (10 μM) or Lyso-OA (10 μM) in the media. Cell death was analyzed using Sytox-green assay ($n = 3$, two-way ANOVA with Tukey's multiple comparison test). (**D** and **E**) Crystal violet staining assays and cytotoxicity analysis of M229R cells treated with IKE (1.25 μM, 24 hours) after 3 days of incubation with CM from M229 cells, with or without Lyso-AA (20 μM) or Lyso-OA (20 μM) in the media ($n = 3$, two-way ANOVA with Tukey's multiple comparison test. NM, normal media; CM, conditioned media). (**F**) Representative Western blot showing the change in expression of AXL, MITF, and GPX4 following 3 and 6 days of treatment with rhApoE3 (200 μM). (Right) Quantification of Western blot showing fold change in the expression of AXL, MITF, and GPX4 relative to untreated control ($n = 3$, one sample *t* test). (**G**) Representative Western blot showing the change in expression of AXL, MITF, and GPX4 following 6 days of treatment with rhApoE2/4 (200 μM). (**H**) Bar plot showing change in expression of *GPX4* level analyzed by qPCR following 6 days of treatment with rhApoE3 (200 μM) relative to untreated control ($n = 3$). (**I** to **K**) Representative Western blot showing the change in expression of NRF2 following 6 days of treatment with rh-ApoE3/ApoE2/ApoE4 (200 μM). Quantification of Western blot showing fold change in NRF2 expression relative to untreated control ($n = 2$ for rhApoE3 and rhApoE2, $n = 3$ for rhApoE4, one sample *t* test). All data represent means ± SEM. $^*P < 0.05$, $^{**}P < 0.01$, $^{***}P < 0.01$, $^{****}P < 0.0001$.

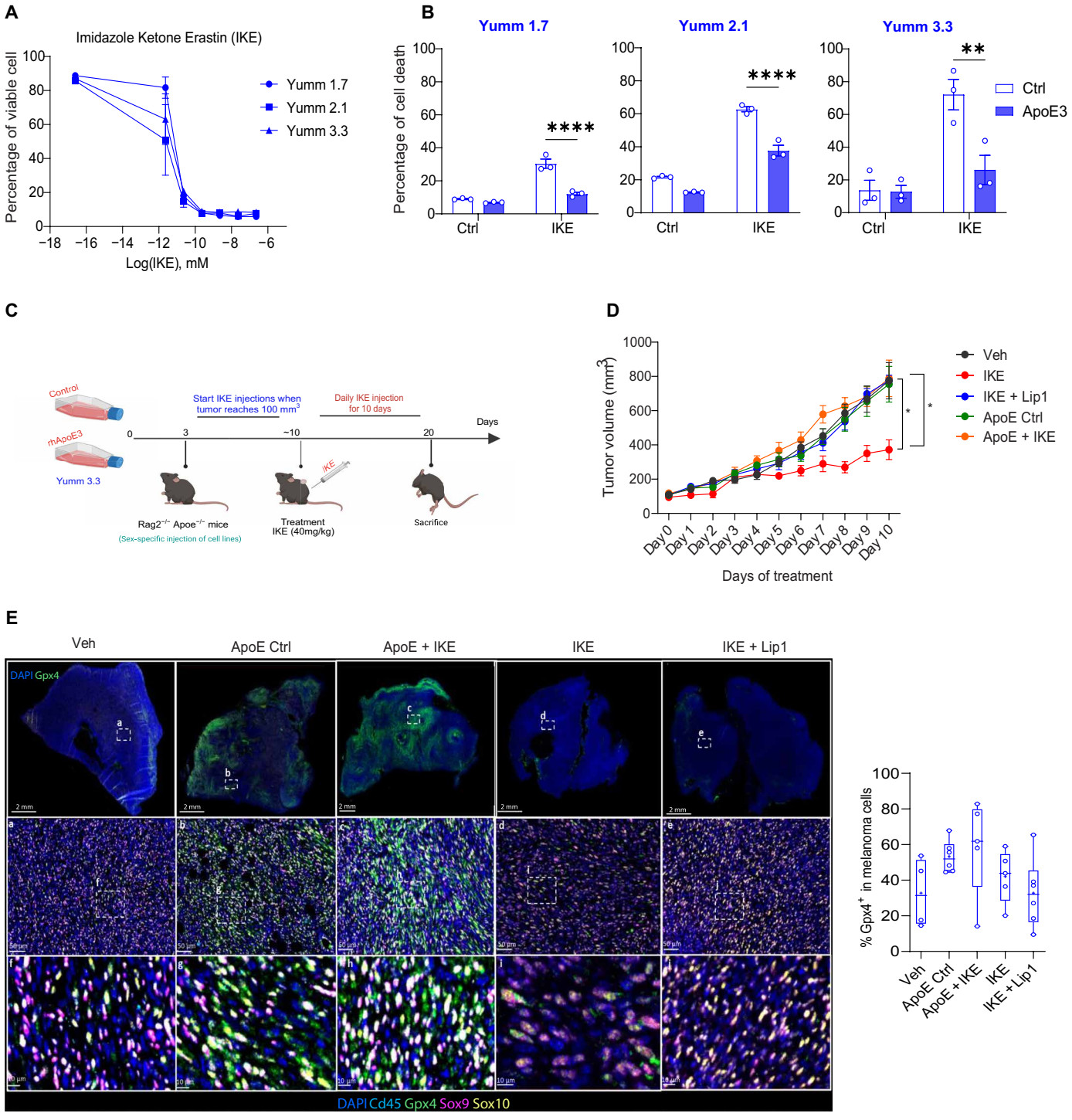

Fig. 6. Melanoma-associated sApoE increases resistance to ferroptosis in vivo. (**A**) Dose curve response showing the sensitivity of murine melanoma cell lines toward IKE. Cells were treated with the indicated concentration of IKE for 24 hours, and cell death was analyzed using Sytox-green assay ($n = 3$). (**B**) Bar plot showing the effect on the sensitivity of Yumm 1.7, Yumm 2.1, and Yumm 3.3 cells toward IKE (0.625 μM, 24 hours) after 3 days of treatment with rhApoE3 (200 μM). Cell death was analyzed using Sytox-green assay ($n = 3$, two-way ANOVA with Tukey's multiple comparison test). (**C**) Schematic description of the in vivo experiment (created with BioRender.com). (**D**) Tumor growth curve in response to 10 days of treatment with IKE (40 mg/kg) in $Rag2^{-/-}$ $Apoe^{-/-}$, C57BL/6 female mice subcutaneously injected with YUMM 3.3 murine melanoma cell line treated or untreated with rhApoE3 (one-way ANOVA with Tukey's multiple comparison test calculated for end time point). (**E**) (Left) Representative images of the Gpx4 (green) staining on tumors across the different conditions. The proportion of $Gpx4^+$ cells was assessed among the $Cd45^-Sox10^{+/-}Sox9^{+/-}$ cancer cells. (Right) Bar plot showing the percentage of $Gpx4^+$ cells among the $Cd45^-$ $Sox10^{+/-}$ $Sox9^{+/-}$ fraction across different conditions.

the involvement of ferroptosis. Of note, the antimelanoma effects of IKE were similarly blunted in rhApoE3-treated Yumm 3.3 melanomas, further supporting the ability of ApoE to suppress ferroptosis in these tumors (Fig. 6D and fig. S6D).

Intrigued by the long-term in vitro effects of sApoE on GPX4 levels, we then stained for Gpx4 in these tumors. Despite a certain variability across samples, we observed a clear trend indicating that Gpx4 protein levels increased in rhApoE3-melanomas both in untreated conditions and following IKE (Fig. 6E), whereas this was not the case in the parental, ApoE3-untreated, Yumm 3.3 melanomas (Fig. 6E). This suggests that the elevated Gpx4 levels induced by sApoE in vivo contribute to the ferroptosis resistant phenotype of these melanomas. Together, these data support the role of sApoE as a regulator of GPX4 expression and ferroptosis resistance in invasive melanoma.

APOE expression is a biomarker of ferroptosis resistance in melanoma irrespective of its germline variant status

Patients with melanoma harboring the *APOE4* genetic variant have improved survival compared with carriers of the *APOE2* and *APOE3* variants (*46*). Mice carrying the human *APOE4* variant exhibited reduced melanoma progression and metastasis relative to *APOE2*- and *APOE3*-bearing mice (*46*). However, it is unknown whether the *APOE* germline genotype predicts susceptibility to ferroptosis in patients with melanoma. We interrogated the SKCM cohort from TCGA database mining the whole-genome sequencing data from 469 melanoma patient samples (Fig. 7A). We identified *APOE* variant status in 445 samples. We then constructed a ferroptosis score (FPS) model to quantify the ferroptosis sensitivity status of patients with melanoma based on ferroptosis-related genes mined from the FerrDB database, which could allow to distinguish ferroptosis sensitivity in melanoma samples based on their differentiation status. Consistent with the data in melanoma cells, melanomas of patients annotated as PRO exhibited low FPS, while INV melanomas had a high FPS (Fig. 7B). Congruently with the in silico analysis described earlier (Fig. 2D), patients harboring the PRO melanoma subtype also exhibited high *APOE* levels ($APOE^{high}$), while melanomas of the INV phenotype had a low level of *APOE* ($APOE^{low}$) (Fig. 7C). Although we did not detect a significant difference in the expression of *GPX4*, there was a trend toward high *GPX4* expression among patients with the PRO melanoma subtype (Fig. 7D).

Exploring the association between melanoma *APOE* variants and their respective FPS revealed no significant difference (Fig. 7E). However, the expression of *APOE* irrespective of the variant status showed a negative correlation with FPS, with significantly lower FPS in samples with higher *APOE*, while, opposite to that, $APOE^{high}$ melanomas had low FPS (Fig. 7, F to H). Furthermore, we found a trend toward a significant positive correlation between *APOE* and *GPX4* expression in melanoma (Fig. 7I). Congruently, the association between FPS and *GPX4* expression also showed a negative trend, thus validating the predictive value of the score (Fig. 7J). This analysis suggests that high expression of *APOE*, irrespective of its variants, serves as a biomarker of ferroptosis resistance in melanomas.

DISCUSSION

We identified the lipoprotein binding protein ApoE as a mediator of ferroptosis resistance between melanoma phenotypes. We integrated in silico, mechanistic, and in vivo data in a model that explains how autocrine secretion of ApoE curbs the induction and propagation of ferroptosis in invasive melanoma cells.

We show that *APOE*, a member of the cholesterol metabolism pathway, is one of the top genes differentiating melanoma cell states at the level of lipid metabolism and whose expression follows the dynamic evolution of melanoma states under therapeutic pressure. The ApoE-lipoprotein complex has been shown to alter the lipid profile of cancer and noncancerous cells (*47*–*49*). However, previous studies did not address the role of secreted ApoE in lipid peroxidation–driven ferroptosis. Our pharmacogenomic analysis revealed a strong correlation between *APOE* expression and ferroptosis susceptibility in melanoma cells. We found that the coexistence of $MITF^{high}ApoE^{high}$ PRO cells with $MITF^{low}ApoE^{low}$ INV melanoma cells is associated with resistance to ferroptosis, which can be reverted by the addition of ApoE-neutralizing antibody, thus revealing a mechanism of ferroptosis resistance between melanoma states.

Recent studies indicated that melanoma progression is dependent on the *APOE* germline variant, and mice carrying the human *APOE4* genetic variant (*hAPOE4*) showed an increased ability to repress Yumm3.3 melanoma growth and metastasis relative to *hAPOE2*- and *hAPOE3*-carrying mice (*46*). Our study shows that the anti-ferroptosis effect of *APOE* correlates with its expression, but it is independent of *APOE*-genetic variant. In line with this, all three variants of ApoE were able to reduce ferroptosis in invasive melanoma cells and elevate GPX4 expression while reducing the invasive marker AXL, suggesting that *APOE* may serve as a biomarker for identifying patients who could benefit from ferroptosis-inducing drugs. Further mechanistic insights into the anti-ferroptosis role of sApoE revealed that it occurs first through the remodeling of the lipidome of the mesenchymal-like cell state. A secondary sApoE-mediated response leads to the sustained expression of GPX4 and a concomitant, partial reversion of the invasive cell state.

We show that both the lipid-binding and receptor binding domains of sApoE are essential to convey ferroptosis resistance. In line with this, binding to LDLR is required by ApoE to perform its downstream effector function (*50*–*52*). There are seven members in the family of LDLR in mammals. In melanoma, ApoE is known to modulate the metastatic potential of melanoma cells by engaging with LRP1 and LRP8 receptor proteins (*21*). While LRP1 is known to control cPLA2 activation and the consequent intracellular levels of AA via the MAPK signaling pathway (*53*), LRP8 has been recently shown to affect ferroptosis by regulating the level of selenoprotein GPX4 in cancer cells (*54*–*56*). A recent study indicated that in melanoma cells, particularly the ApoE2 isoform among the top up-regulated pathways, increased the expression of genes involved in selenoamino acid metabolism and protein translation machinery (*57*). This mechanism could therefore link the ApoE-LRP1/8 axis to the increased expression of the selenoprotein GPX4 and the acquired ferroptosis resistance of INV melanoma cells disclosed by our work.

The anti-ferroptosis role of melanoma sApoE is likely mediated by the activation of signaling pathways downstream of these receptors, although the specific LDLR involved needs to be addressed in further studies. In addition, we cannot exclude that other ApoE-mediated mechanisms, such as the ability to directly bind iron (*58*) or block the autophagic degradation of ferritin (*59*), contribute to its anti-ferroptosis action in invasive melanoma.

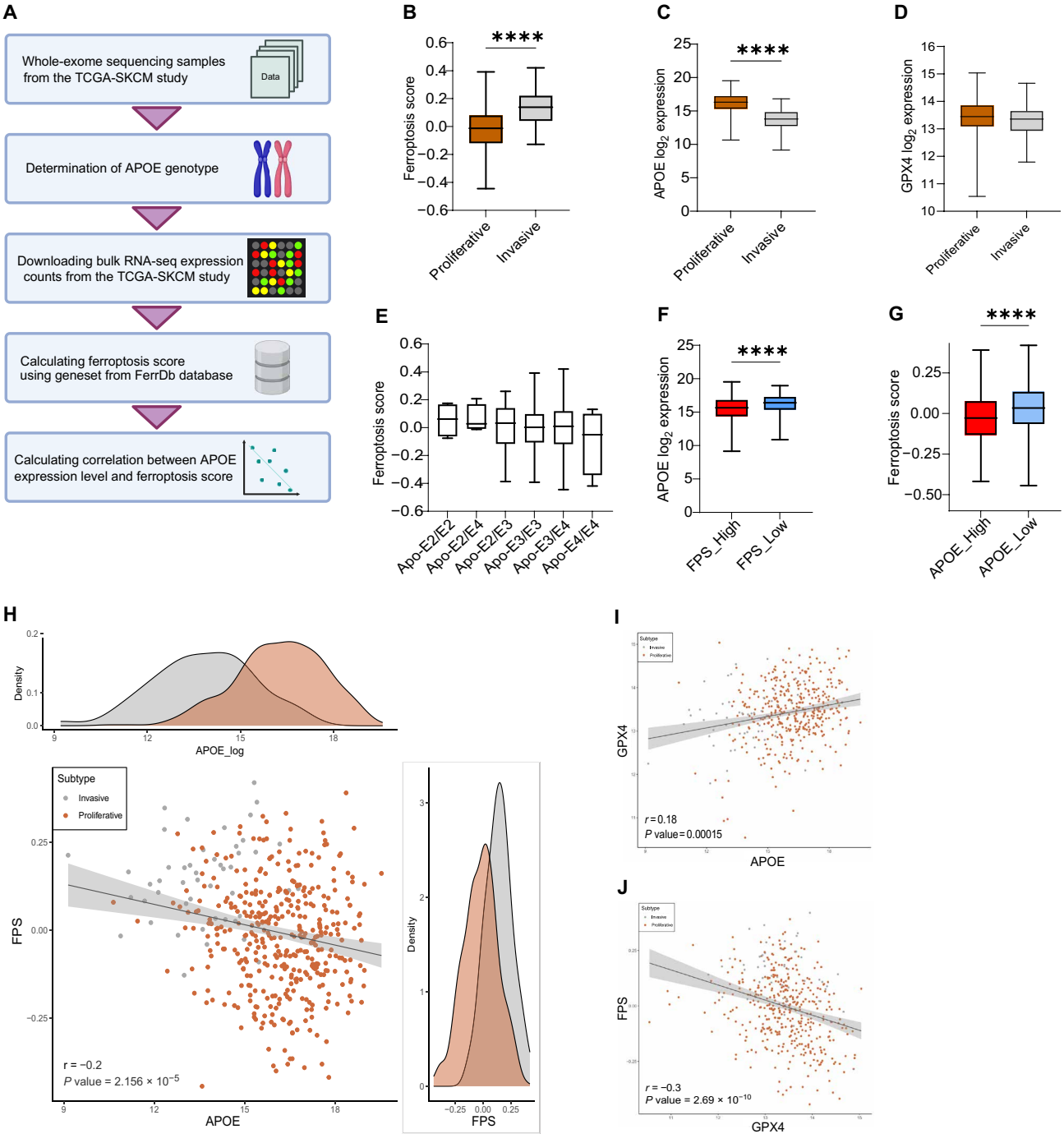

Fig. 7. APOE expression is a biomarker of ferroptosis resistance in melanoma irrespective of its germline variant status. (**A**) Schematic representation showing computational pipeline used to analyze the correlation between *APOE* genotype variant and ferroptosis sensitivity in the TCGA-SKCM study. (**B**) Box plot showing FPS values in TCGA-SKCM patient samples annotated as proliferative and invasive (unpaired Mann-Whitney test). (**C** and **D**) Box plots showing the expression of *APOE* and *GPX4* ($\log_2$ transformed) in TCGA-SKCM patient samples annotated as proliferative and invasive (unpaired Mann-Whitney test). (**E**) Box plot showing FPS values in TCGA-SKCM patient samples with different *APOE* variants (unpaired Mann-Whitney test). (**F**) Box plot showing FPS values in TCGA-SKCM patient samples with high and low *APOE* levels (unpaired Mann-Whitney test). (**G**) Box plot showing the expression of *APOE* ($\log_2$ transformed) in TCGA-SKCM patient samples with high and low FPS values (unpaired Mann-Whitney test). (**H**) Scatter plot merged with density plots showing a correlation between the expression of *APOE* ($\log_2$ transformed) and FPS in TCGA-SKCM dataset. The density plot above shows the expression of *APOE* in patient samples annotated as proliferative and invasive. Density plot on the right show FPS in patient samples annotated as proliferative and invasive (r = value of Spearman correlation). (**I**) Scatter plot showing a correlation between expression of *GPX4* and *APOE* ($\log_2$ transformed) in TCGA-SKCM dataset annotated as proliferative and invasive (r = value of Spearman correlation). (**J**) Scatter plot showing a correlation between expression of *GPX4* ($\log_2$ transformed) and FPS in TCGA-SKCM dataset annotated as proliferative and invasive ($_r$ = value of Spearman correlation). *$P < 0.05$, **$P < 0.01$, ***$P < 0.01$, ****$P < 0.0001$.

Our lipidomics and cell biology analysis revealed that sApoE3 reduced cPLA2 enzymatic activity, likely by lessening intracellular Ca^{2+} levels and, correspondingly, dampened the levels of Lyso-PLs in the INV cells. Consistent with this, supplementing Lyso-PUFAs to sApoE-treated invasive cells rescued their ferroptosis vulnerability, whereas Lyso-MUFAs failed to do so. The calcium-dependent cPLA2α cleaves AA at the sn-2 position of glycerophospholipids to release AA from the membrane and may promote ferroptosis through the iron- and LOX-dependent accumulation of lethal lipid peroxides following ASCL4- and LPCAT3-mediated PE re-esterification. Consistent with our results, a recent study showed that in neuronal cells, thrombin mediated increases in cPLA2α activity sensitized these cells to ferroptosis in an ASCL4-dependent manner (*31*). In contrast, inhibition of the calcium-independent iPLA2β, which cleaves acyl tails from the glycerol backbone of lipids, fostered p53-driven ferroptosis and tumor suppression by depleting the pool of oxidized lipids in response to ROS-generating drugs (*28*). These findings suggest that blockade of cPLA2α or iPLA2β may differentially affect ferroptosis outcome by regulating the oxidized status of the intracellular AA pool. Following the initial remodeling of the Lyso-PUFAs pool, prolonging the exposure of invasive cells to sApoE increased the levels of GPX4 in both ferroptosis-sensitive human cells in vitro and mouse melanoma cells in vivo.

Several transcription factors including AP-1 (*60*, *61*), CREB (*62*, *63*), ATF4 (*64*), and NRF2 (*45*, *65*, *66*) have been shown to regulate either directly or indirectly GPX4 levels in different cellular contexts. Given the pleiotropic signaling effects elicited by sApoE downstream LDLR binding, it is likely that multiple transcription factors contribute to elevating GPX4 expression in invasive melanoma cells. Notwithstanding the exact molecular mechanism by which sApoE triggers the GPX4 signal warrants further studies, our in vivo data support the anti-ferroptosis role of this sApoE-regulated pathway.

Prolonged exposure of invasive melanoma cells to sApoE also decreased AXL levels, suggesting the ability to partially revert the INV phenotype, at least under these settings. In contrast, the MITF status was not consistently changed by sApoE. However, while loss of MITF is sufficient to induce the invasive phenotype, the transition from an invasive to a proliferative phenotype requires the integration of additional signals and epigenetic modifications capable of stably rescuing MITF-driven transcription of proliferation and differentiation genes (*67*). Of note, sApoE has been found to influence the transcriptome by modulating histone acetylation (*68*, *69*). Whether additional tumor microenvironmental factors endorse ApoE-mediated transition of the drug-resistant invasive melanoma state to a proliferative phenotype is an intriguing possibility that warrants future studies.

In conclusion, we show that secreted ApoE functions as an autocrine ferroptosis suppressor in melanoma. Given the emerging evidence of ferroptosis as a promising strategy to treat drug-resistant melanoma tumors, our findings suggest that the use of ApoE-neutralizing therapy in combination with ferroptosis-inducing agents may be of potential benefit.

MATERIALS AND METHODS

Reagents

IKE (1801530-11-9), RSL-3 (1219810-16-8), Lip-1 (950455-15-9), Fer-1 (347174-05-4), Piroxicam (36322-90-4), MSPPOH (206052-02-0), PD146176 (4079-26-9), ML355 (1532593-30-8), AA (506-32-1), ATK (149301-79-1), OA (112-80-1), SSO (1212012-37-7), and lipofermata (297180-15-5) were purchased from Cayman. DFO (138-14-7), varespladib (172732-68-2), dimethyl sulfoxide (67-68-5), Tween-80 (9005-65-6), polyethylene glycol 400 (25322-68-3), lipoprotein-deficient serum from fetal calf (S5394), and D-(+)-glucose (50-99-7) were purchased from Sigma-Aldrich. Sytox Green (S7020), Viability Dye eFluor 780 (65-0865-14), and C11BODIPY (D3861) were purchased from Thermo Fisher Scientific. Nec-1s (2263) was purchased from BioVision. Darapladib (356057-34-6) was purchased from Selleckchem. Lysis solution (G1821) was purchased from Promega. Recombinant human apolipoprotein E2 (ab123749), E3 (ab123764), E4 (ab123766), and phospholipase A2 activity assay kit (ab273278) were purchased from Abcam. Anti-Apo E (1D7), human IgG1, Fc Silent, and Kappa (Ab01194-10.3) were purchased from Absolute Antibody. APOE enzyme-linked immunosorbent assay (ELISA) kit (Innovative Research), recombinant human apolipoprotein E3 variant 1-191 (C-terminal truncated), and variant 192-299 (N-terminal truncated) were custom-made through AlexoTech.

Cell lines

Human melanoma cell line WM35 was obtained from American Type Culture Collection. Human melanoma cell lines M229, M229 R, M238, M238 R, M249, and M249 R were provided by R. Lo (UCLA); WM852 was a gift of M. Herlyn (The Wistar Institute); and M263, M233, M257, and M308 were a gift of A. Ribas (UCLA). All the cell lines were maintained in Dulbecco's modified Eagle's medium (DMEM) (Sigma-Aldrich) supplemented with 10% (v/v) fetal bovine serum (FBS, PAN-Biotech), 2 mM glutamine (Sigma-Aldrich), penicillin (100 U/ml), and streptomycin (0.1 mg/ml) (Sigma-Aldrich). Cell lines with acquired resistance to vemurafenib (PLX4032/PLX) (M249R, M229R, and M238R) were maintained continuously on 1 μM PLX in cell culture. Murine melanoma cell lines Yumm 1.7, Yumm 2.1, and Yumm 3.3 were provided by M. Mazzone (VIB-KU Leuven CCB). All the murine cell lines were DMEM/F12 (Sigma-Aldrich) media containing 10% FBS and supplemented with 1% penicillin-streptomycin and 1% nonessential amino acids (Sigma-Aldrich). All cells were maintained routinely in 5% CO_2 and 95% air at 37°C. The cells were routinely checked for mycoplasma contaminations using the Plasmotest kit (Invivogen) according to the manufacturer's instructions.

3D spheroid models

To create the spheroids, 4000 cells per well were seeded for 3 days in nonadherent 96-well plates (Nucleon Sphere plates from Thermo Fisher Scientific). For the heterotypic spheroids, 60%-2400 cells per well and 40%-1600 cells per well of M229R and M229 cells were seeded, respectively. After 3 days, spheroids were treated with IKE (10 μM; a higher concentration was required as compared to 2D condition to induce measurable cell death and lipid peroxidation) ± Lip-1 for 24 hours (six spheroids per condition). After 24 hours, spheroids from the same condition were pooled, washed (5 min at 300 g), and trypsinized (5 min at 37°C) to obtain a single-cell suspension. Then, the cells were stained for flow cytometry analysis with eFluor780 Live/Dead dye and Bodipy C11 for 30 min. The cells were analyzed with the BD LSFortessa X-20 + HTS flow cytometer. For microscopic analysis, the spheroids pellet were gently resuspended in 15 μl of GelTrex without destroying them, dropped in a

glass-bottom petri dish, and incubated for 20 min at 37°C for GelTrex polymerization. After incubation, 1 ml of RPMI 1640 medium was added to recover the droplet, and the petri dish was immediately imaged with a confocal microscope (20× magnification). The images were processed using Icy software.

Immunoblotting

Hepes lysis buffer containing protease and phosphatase inhibitor was used to lysate cells. Protein concentration in cell lysates was determined using the bicinchoninic acid protein assay reagent (Pierce, Thermo Fisher Scientific). The cell lysates were loaded on bis-tris gel (4 to 12%) and separated by SDS–polyacrylamide gel electrophoresis on the Criterion system (Bio-Rad Laboratories). Samples from the gel were electrophoretically transferred to the nitrocellulose membrane. The membranes were blocked for 1 hour at room temperature in TBS-T buffer [50 mM tris (pH 7.4), 150 mM NaCl, and 0.1% Tween-20] containing 5% nonfat dry milk (w/v). Following blocking, the membranes were incubated with the appropriate primary antibody in blocking buffer overnight at 4°C. After three washes with TBS-T buffer, the membranes were incubated with horseradish peroxidase (HRP)–conjugated secondary antibody for 1 hour at room temperature in blocking buffer. Protein bands were visualized using an Amersham ECL imager.

Primary antibodies for AXL (1:1000, #8661), MITF (1:1000, #12590), APOE (1:500, #13366), and β-actin (1:2000, #3700) were purchased from the Cell Signaling Technology. GPX4 (1:500, #MAB5457) was purchased from Bio-techne. NRF2 (1:1000, #31163) was purchased from Abcam. Secondary anti-rabbit (1:2000 dilution, #7074S) and anti-mouse antibodies (1:2000, #7076S) were purchased from Cell Signaling Technology.

Flow cytometry

To assess cell death, the cells were treated with indicated concentrations of FINs and then collected by trypsinization and stained with eFluor 780 viability dye. Fluorescence was measured using the BD FACSymphony A1 Cell Analyzer. For lipid peroxidation analysis, the cells were treated with the indicated concentration of FINs for the mentioned period and then collected by trypsinization and stained with BODIPY 581/591 C11 dye for 30 min at 37°C. Fluorescence was measured using the BD FACSCanto II. The percentage of lipid peroxidation was analyzed by observing a shift in the Bodipy C11 fluorescence in the fluorescein isothiocyanate channel compared to the unstained cell. Data were analyzed using FCS Express 7 software.

Crystal violet, cytotoxicity, and cell viability assay

For the crystal violet assay, the cells were plated in six-well plates for treatment according to the experimental conditions; after the required days of treatment, the cells were washed with cold phosphate-buffered saline (PBS) and incubated with 10% methanol for 10 min on a shaker at room temperature. The cells were stained with crystal violet solution (1% crystal violet and 50% methanol) for 10 min and washed with water until the dye stopped coming off. To analyze the cytotoxicity of the treatment on cells, the crystal violet dye was solubilized using 10% acetic acid, and the absorbance was measured at 570 nm. Calculation of the percentage of cytotoxicity was done using the formula below

$$\%Cytotoxicity = OD\ DMSO - OD\ sample/OD\ DMSO \times 100\%$$

The effect on the viability of cells seeded in 96-well plates upon treatment with FINs and/or other compounds was analyzed using the SYTOX Green assay. Briefly, SYTOX Green was added to cells at the final concentration of 1 μM, together with compounds whose effect on the viability of cells need to be checked, and in the control wells, fluorescence was measured after 24 hours using the BioTek Synergy H1 Microplate Reader at 485 ex/538 em. After the first fluorescence measurement, the cells were lysed by adding lysis buffer for 10 min at 37°C. The second fluorescence measurement was taken after 10 min, and the percentage of cell death was calculated by using the formula: before lysis measurement (first measurement) / after lysis measurement (second measurement) *100%.

Generation of genetically modified cell lines

Lentiviral short hairpin RNA (shRNA) vector against human MITF was purchased from Sigma-Aldrich, and APOE was custom prepared with Sigma-Aldrich (table S4). An empty pLKO.1-puro control vector was used as a control (shCntl). To generate lentiviral particles, human embryonic kidney 293T cells were seeded in 10-cm^2 dishes at 1.5×10^6 cells per 6 ml and transfected the following day by the calcium phosphate method with 4 μg of pLKO.1-puro carrying the respective shRNAs or with empty pLKO.1-puro. Each transfection also included 1.2 μg of a plasmid encoding vesicular stomatitis virus glycoprotein (VSV-G, pMD2-VSV-G, Tronolab) and 2.6 μg of a plasmid encoding packaging proteins (pCMVdR8.9, Tronolab). VSV-G pseudotyped virus was collected 48 hours after transfection, passed through 0.45-μm filters (Millipore, Burlington, MA, USA), and then added to the exponentially growing melanoma cell cultures in the presence of polybrene (8 mg/ml). The cells were expanded and selected by puromycin treatment (10 μg/ml). Target downregulation was confirmed by immunoblotting. The lentivirus expressing EBFP and mCherry plasmid were gifted by G. Bergers laboratory. The melanoma cells (M229R with EBFP and M229 with mCherry) were transduced with lentiviral particles for 48 hours in the presence of polybrene (8 mg/ml). The cells were expanded and selected by puromycin treatment (10 μg/ml). After 3 weeks of culturing, the cells were FACS sorted to select cells expressing high levels of EBFP and mCherry, respectively, using BD FACSAria cell sorter.

Quantitative real-time polymerase chain reaction

RNA extraction was performed using RNeasy Plus mini kit (74136, Qiagen) and reverse transcribed using QuantiTect (205313, Qiagen) kit. Expression of genes was determined using ORA quantitative polymerase chain reaction Green L mix (QPD0105, HighQu) with the ABI 7500 machine (Applied Biosystems) and analyzed using the Δ ΔCt method. Primer sequences are available in table S4.

ApoE ELISA

Conditioned media from melanoma cell lines was prepared by culturing the cells with 70% confluency in 0.2% FBS culture media for 24 hours Secreted ApoE level in conditioned media was quantified using the APOE ELISA kit according to the manufacturer's protocol.

PLA2 activity assay

The cPLA2 activity was analyzed using phospholipase A2 activity assay kit (#ab273278) from Abcam. Cells (125,000 cells) were seeded in a 5-cm^2 plate and treated with or without rhApoE3 for 3 days. After 3 days, the cells were washed with cold PBS and collected using

a cell scraper. The cells were lysed in assay buffer and centrifuged at 10,000*g* for 10 min at 4°C. The supernatant was transferred to a prechilled microcentrifuge tube and treated with bromoenol lactone and darapladib for 10 min at 25°C to avoid measurement of iPLA2 and lpPLA2 activity, respectively, in the sample. Next, the sample was analyzed according to the manufacturer's protocol, and the data were normalized to the protein concentration.

Calcium assay

Intracellular calcium in the cells was analyzed by using Fluo-8 Calcium Flux Assay Kit (#ab112129) from Abcam. The cells were seeded in black 96-well plates, and after treatment with rhApoE3 for 3 days, 100 µl of Fluo-8 dye-loading solution was added to the wells according to the manufacturer's protocol. Next, the plate was incubated at 37°C (in incubator) for 30 min and then at room temperature for another 30 min. The intracellular calcium level was measured by monitoring the fluorescence intensity using the BioTek Synergy H1 Microplate Reader at 490 ex/525 em. The intensity values were normalized to the amount of protein.

Lipidomics analysis

For bulk lipidomic analysis, melanoma cells were cultured in complete serum media for 48 hours. The cells were washed twice with cold PBS and collected using a cell scraper in prechilled falcon tubes. The cells were pelleted by centrifuging at 1000 rpm for 5 min at 4°C and subjected to lipidomic analysis. Lipidomic analysis was performed on collected cells as described previously (*70*). Normalization of data was done on DNA amount.

Patient sample acquisition and processing

The use of from melanoma patients samples for the present study was approved by the Medical Ethics Committee of the UZ Leuven/KU Leuven (HBM) (approval number, S66737). Briefly, 5-µm-thick sections of OCD-embedded frozen tumor samples were collected onto Superfrost Plus slides and subjected to RNAscope and Spatial lipidomic analysis.

Fluorescence in situ hybridization using RNAscope

Sections (5-µm-thick) of frozen tumor samples from patients with melanoma were collected onto Superfrost Plus slides. Multiplex fluorescence in situ hybridization was performed using the RNAscope Multiplex Fluorescent V2 Assay kit (ACDBio, 323100), reagents, and probes according to the manufacturer's protocol. RNAscope probes were designed commercially by the manufacturer and are available through Advanced Cell Diagnostics. The following probes were used: MITF (310951-T1) and APOE (433091-T7) for humans. The probes were then labeled with TSA opal 520 (PerkinElmer, FP1487001KT) and TSA opal 570 (PerkinElmer, FP1488001KT). The samples were counterstained with 4′,6-diamidino-2-phenylindole (DAPI) for 5 min and mounted with ProLong Gold Antifade Mountant (Thermo Fisher Scientific, P36930). The tissue was segmented from background using Otsu thresholding, removing nonspecific imaging artefacts. Multiple RNAscope imaging cycles were aligned using SimpleITK (version 2.2.1). Cycles were registered onto a reference cycle using first a linear rigid transformation, followed by a more fine-grained nonlinear B-spline transformation. The cells were segmented using QuPath's cell detection module. The cells were assigned as MITF high/low based on fluorescence intensity. Autofluorescence was subtracted from each image channel using a cycle-specific autofluorescence channel. APOE expression per cell was assigned by measuring their average intensity in the APOE channel. Extreme outliers with an APOE expression of more than 3 SDs from the mean were removed from further calculations. Difference of APOE expression between the MITF high/low populations was expressed as the difference in their respective means. Statistical testing was done using scipy.stats.ttest_ind (version 1.9.1).

Animal studies

Animal procedures were approved by the Institutional Animal Care and Research Advisory Committee of the KU Leuven (ECD P073/2020) and were performed following the institutional and national guidelines and regulations. Breeding pair of C57BL/6 Apoe$^{-/-}$ Rag2$^{-/-}$ mice was gifted by the laboratory of B. De Strooper. To monitor the subcutaneous tumor growth, 500,000 Yumm 3.3 cells murine melanoma cells were subcutaneously injected into the right flanks of 6- to 10-week-old female mice, with Matrigel in a 1:1 ratio with or without rhApoE3 (100 µg/ml). Once the tumor reached a volume of 100 mm^3, the mice were treated with daily intraperitoneal injections of vehicle (65% D5W, 30% PEG400, and 5% Tween-80), IKE (40 mg/kg), or IKE plus Lip-1 (20 mg/kg) for 10 days. The mice were weighed, and tumor volumes were measured every day after reaching 100 mm^3 with a caliper using the formula $V = \pi * [D*d*t]/6$, where D is the major tumor axis, d is the minor tumor axis, and t is the thickness of the tumor. The mice were euthanized after 10 days of treatment or when the tumors reached a maximum size of 1000 mm^3 depending on the experimental setup.

Immunoflurescence stainings

Tissue samples from representative lesions were collected and fixed in 4% paraformaldehyde for 24 hours and then processed for paraffin embedding (HistoStar Embedding Workstation). Sections of 4 µm of thickness obtained from the paraffin-embedded tissues (Thermo Fisher Scientific Microm HM355S microtome) were mounted on Superfrost Plus Adhesion slides (Thermo Fisher Scientific). The following antibodies were used for detecting the respective proteins: anti-Sox10 (rabbit, 1:600, Abcam, ab155279), anti-SOX9 (rabbit, 1:500, Abcam, ab185230), anti-GPX4 (rabbit, 1:200, PA5-109274), and anti-CD45 (rabbit, 1:500, Novus, NBP2-15811). Furthermore, the "Opal 6-Plex Detection Kit - for Whole Slide Imaging" (Akoya, NEL871001KT) was used for the tyramide signal amplification according to the manufacturer's protocol. For introduction of the secondary-HRP, the Envision+/HRP goat anti-rabbit (Dako Envision+ Single Reagents, HRP, Rabbit, Code K4003) was used for all antibodies. The various proteins were detected by using the OPAL 520 (Sox10), OPAL 570 (Gpx4), OPAL 620 (Cd45), or OPAL 780 (Sox9) reagents according to the manufacturer's protocol. Images were acquired on the Akoya PhenoImager HT (formerly known as Vectra Polaris) using a ×20 objective without binning. All the images were analyzed with QuPath software. A cell detection was applied on the basis of the DAPI staining: Four different single classifiers were set up for the Gpx4, Sox9, Sox10, and Cd45 staining and sequentially applied on the same slides to assess the proportion of Gpx4$^+$ cells among the tumor cells (CD45-SOX10$^+$/$^-$SOX9$^{+/-}$).

Statistical analysis

Statistical analyses were performed using GraphPad Prism 9 and unpaired Student's *t* test for experiments with two groups. One-way

analysis of variance (ANOVA) was used to compare multiple experimental groups, and two-way ANOVA was used to compare continuous outcomes across multiple experimental groups. For all tests, $P < 0.05$ was considered significant. The sample size was not predetermined. Unless noted, samples were independent biological replicates. All data represent means ± SEM. *$P < 0.05$, **$P < 0.01$, ***$P < 0.01$, ****$P < 0.0001$.

Transcriptomic datasets

Publicly available datasets from Tsoi *et al.* (*10*) was used to analyze transcriptomic changes within lipid metabolism pathways occurring at a different stage of melanoma development, thus regulating ferroptosis vulnerability across different subtype of melanoma (GSE80829). Fragments per kilobase of transcript per million mapped reads (FPKM) values for 53 melanoma cell lines belonging to 4 main subtypes were obtained from GSE80829. FPKM values were $\log_2$ transformed, and hierarchical clustering was performed by calculating Euclidean distance matrix and Ward2 method on a set of 1376 genes involved in lipid metabolism identified through Reactome and KEGG database. FPKM values were $\log_2$ transformed and imported into an online tool "Morpheus" to build a heatmap. An online tool developed by Graeber's laboratory described in Tsoi *et al.* 2018 was used to visualize gene expression trends among the melanoma subtypes within the bulk RNA-seq dataset of TCGA-SKCM in PCA space.

DE analysis

A list of top variables was chosen on the basis of mean differences across the conditions. DE analysis was performed by calculating the fold change. Significance testing between two conditions was performed with a two-sided/tailed *t* test. Values above 1 $\log_2$ fold change and adjusted *P* value less than 0.05 were considered as significantly different.

Overrepresentative analysis

The web tool "WEBGESTALT" was used to perform ORA. The KEGG database was used for pathway enrichment analysis. The *P* value less than 0.05 of false discovery rate tested by the Benjamini and Hochberg method was set as the significance threshold.

Trajectory analysis

Gene expression profile from GSE116237 was used to build a pseudo-time trajectory using Monocle package 2.18.0 in R 4.0.3. Cell-type annotations were provided to us by the authors of the original study. All cells that were not associated with one of the labels (e.g., "other") were discarded. Size factors and dispersion were estimated to select genes of interest with minimal expression of 0.1 in at least 10 cells. The cells were removed if less than 2000 or more than 9000 genes with expression were found. Dimensionality reduction was performed with 2 components on 16 dimensions using t-distributed stochastic neighbor embedding. The cells were assigned to five clusters. For consistency with the original paper (*1*), we used the Ensembl gene IDs provided in table S2 as genes of interest needed to build the trajectory graph. Trajectories were further dissected with the branched expression analysis module in monocle, using node 3 in the graph as a branching point.

CTRP data analysis

The gene expression data for melanoma cell lines [Expression Public 23Q2, $\log_2(\text{TPM} + 1)$ values] and their drug sensitivity area under the curve (AUC) values (CTD^2) were downloaded from depmap-portal. The correlation analysis was performed between the expression of APOE and AUC values of different FINs (1S, 3R, RSL3, ML162, ML210, and Erastin) using the base R stats function cor. test (Spearman). Low AUC values indicate increased sensitivity. All statistical analyses were performed in R (version 4.2.3) and GraphPad Prism 9.

Analysis of APOE genotype and correlation with ferroptosis sensitivity in the TCGA-SKCM dataset

Whole-exome sequencing (WES) BAM files of 469 blood-derived normal samples from the TCGA SKCM cohort (phs000178.v11.p8) were downloaded using the GDC client. The ApoE genotype of each sample was determined with GATK (version 4.1.3.0) HaplotypeCaller, CombineGVCFs, and GenotypeGVCFs using the Genome Reference Consortium Human Build 38 (GRCh38) genome and with "-G AS_StandardAnnotation -G StandardAnnotation" as additional settings to enable allele-specific annotations. Genotype information of SNPs rs429358 and rs7412 was extracted using the vcfR package (version 1.14.0) (*3*). The bulk RNA-seq expression counts were downloaded for all TCGA-SKCM patient samples that had both paired WES and bulk RNA-seq data (in total 467 patient samples). The bulk RNA-seq count files were collated into a count matrix.

To calculate the FPS, we downloaded a set of genes termed suppressor or driver of ferroptosis from the FerrDb database. Only genes with protein product and confidence level as "validate" accordingly to the FerrDb database were selected (table S3). Gene set variation analysis (GSVA) enrichment score for ferroptosis suppressor and driver gene list was calculated for each patient sample using the R Bioconductor package GSVA (version 1.49.0). The FPS to computationally dissect patient samples as ferroptosis sensitive or resistant was defined by the calculating differences in enrichment score between the ferroptosis driver and ferroptosis suppressor. Patients with scores higher than mean FPS were defined as sensitive, and those lower than mean FS were defined as resistant to ferroptosis. The patient samples were annotated as proliferative and invasive based on previous knowledge from Tsoi *et al.* (*10*). Spearman correlations were performed between APOE expression levels and FPS using the base R stats function cor. test. All statistical analyses were performed in R (version 4.2.3) and GraphPad Prism 9.

Supplementary Materials

The PDF file includes:

Figs. S1 to S6

Legends for tables S1 to S5

Other Supplementary Material for this manuscript includes the following:

Tables S1 to S5

REFERENCES AND NOTES

1. F. Rambow, A. Rogiers, O. Marin-Bejar, S. Aibar, J. Femel, M. Dewaele, P. Karras, D. Brown, Y. H. Chang, M. Debiec-Rychter, C. Adriaens, E. Radaelli, P. Wolter, O. Bechter, R. Dummer, M. Levesque, A. Piris, D. T. Frederick, G. Boland, K. T. Flaherty, J. van den Oord, T. Voet, S. Aerts, A. W. Lund, J.-C. Marine, Toward minimal residual disease-directed therapy in melanoma. *Cell* **174**, 843–855.e19 (2018).
2. O. Marin-Bejar, A. Rogiers, M. Dewaele, J. Femel, P. Karras, J. Pozniak, G. Bervoets, N. Van Raemdonck, D. Pedri, T. Swings, J. Demeulemeester, S. V. Borght, S. Lehnert, F. Bosisio, J. J. van den Oord, I. V. Bempt, D. Lambrechts, T. Voet, O. Bechter, H. Rizos, M. P. Levesque, E. Leucci, A. W. Lund, F. Rambow, J.-C. Marine, Evolutionary predictability

of genetic versus nongenetic resistance to anticancer drugs in melanoma. *Cancer Cell* **39**, 1135–1149 (2021).
3. A. Tasdogan, B. Faubert, V. Ramesh, J. M. Ubellacker, B. Shen, A. Solmonson, M. M. Murphy, Z. Gu, W. Gu, M. Martin, S. Y. Kasitinon, T. Vandergriff, T. P. Mathews, Z. Zhao, D. Schadendorf, R. J. DeBerardinis, S. J. Morrison, Metabolic heterogeneity confers differences in melanoma metastatic potential. *Nature* **577**, 115–120 (2020).
4. M. Zhang, J. S. Di, Martino, R. L. Bowman, N. R. Campbell, S. C. Baksh, T. Simon-Vermot, I. S. Kim, P. Haldeman, C. Mondal, V. Yong-Gonzales, M. Abu-Akeel, T. Merghoub, D. R. Jones, X. G. Zhu, A. Arora, C. E. Ariyan, K. Birsoy, J. D. Wolchok, K. S. Panageas, T. Hollmann, J. J. Bravo-Cordero, R. M. White, Adipocyte-derived lipids mediate melanoma progression via fatp proteins. *Cancer Discov.* **8**, 1006–1025 (2018).
5. P. Karki, S. Sensenbach, V. Angardi, M. A. Orman, BRAF-inhibitor-induced metabolic alterations in A375 melanoma cells. *Metabolites* **11**, 777 (2021).
6. V. S. Viswanathan, M. J. Ryan, H. D. Dhruv, S. Gill, O. M. Eichhoff, B. Seashore-Ludlow, S. D. Kaffenberger, J. K. Eaton, K. Shimada, A. J. Aguirre, S. R. Viswanathan, S. Chattopadhyay, P. Tamayo, W. S. Yang, M. G. Rees, S. Chen, Z. V. Boskovic, S. Javaid, C. Huang, X. Wu, Y.-Y. Tseng, E. M. Roider, D. Gao, J. M. Cleary, B. M. Wolpin, J. P. Mesirov, D. A. Haber, J. A. Engelman, J. S. Boehm, J. D. Kotz, C. S. Hon, Y. Chen, W. C. Hahn, M. P. Levesque, J. G. Doench, M. E. Berens, A. F. Shamji, P. A. Clemons, B. R. Stockwell, S. L. Schreiber, Dependency of a therapy-resistant state of cancer cells on a lipid peroxidase pathway. *Nature* **547**, 453–457 (2017).
7. S. J. Dixon, K. M. Lemberg, M. R. Lamprecht, R. Skouta, E. M. Zaitsev, C. E. Gleason, D. N. Patel, A. J. Bauer, A. M. Cantley, W. S. Yang, B. Morrison, B. R. Stockwell, Ferroptosis: An iron-dependent form of nonapoptotic cell death. *Cell* **149**, 1060–1072 (2012).
8. J.-Y. Lee, W. K. Kim, K.-H. Bae, S. C. Lee, E.-W. Lee, Lipid metabolism and ferroptosis. *Biology* **10**, 184 (2021).
9. F. Baenke, B. Peck, H. Miess, A. Schulze, Hooked on fat: The role of lipid synthesis in cancer metabolism and tumour development. *Dis. Model. Mech.* **6**, 1353–1363 (2013).
10. J. Tsoi, L. Robert, K. Paraiso, C. Galvan, K. M. Sheu, J. Lay, D. J. L. Wong, M. Atefi, R. Shirazi, X. Wang, D. Braas, C. S. Grasso, N. Palaskas, A. Ribas, T. G. Graeber, Multi-stage differentiation defines melanoma subtypes with differential vulnerability to drug-induced iron-dependent oxidative stress. *Cancer Cell* **33**, 890–904.e5 (2018).
11. C. Kosnopfel, T. Sinnberg, B. Sauer, H. Niessner, A. Muenchow, B. Fehrenbacher, M. Schaller, P. R. Mertens, C. Garbe, B. K. Thakur, B. Schittek, Tumour progression stage-dependent secretion of YB-1 stimulates melanoma cell migration and invasion. *Cancers* **12**, 2328 (2020).
12. G. Li, H. Schaider, K. Satyamoorthy, Y. Hanakawa, K. Hashimoto, M. Herlyn, Downregulation of E-cadherin and Desmoglein 1 by autocrine hepatocyte growth factor during melanoma development. *Oncogene* **20**, 8125–8135 (2001).
13. E. J. Ekström, C. Bergenfelz, V. von, Bülow, F. Serifler, E. Carlemalm, G. Jönsson, T. Andersson, K. Leandersson, WNT5A induces release of exosomes containing pro-angiogenic and immunosuppressive factors from malignant melanoma cells. *Mol. Cancer* **13**, 88 (2014).
14. C. Levy, M. Khaled, D. E. Fisher, MITF: Master regulator of melanocyte development and melanoma oncogene. *Trends Mol. Med.* **12**, 406–414 (2006).
15. J. Wu, A. M. Minikes, M. Gao, H. Bian, Y. Li, B. R. Stockwell, Z.-N. Chen, X. Jiang, Publisher correction: Intercellular interaction dictates cancer cell ferroptosis via NF2-YAP signalling. *Nature* **572**, E20 (2019).
16. J. Du, Y. Su, C. Qian, D. Yuan, K. Miao, D. Lee, A. H. C. Ng, R. S. Wijker, A. Ribas, R. D. Levine, J. R. Heath, L. Wei, Raman-guided subcellular pharmaco-metabolomics for metastatic melanoma cells. *Nat. Commun.* **11**, 4830 (2020).
17. H. J. Lee, Z. Chen, M. Collard, F. Chen, J. G. Chen, M. Wu, R. M. Alani, J.-X. Cheng, Multimodal metabolic imaging reveals pigment reduction and lipid accumulation in metastatic melanoma. *BME Front.* **2021**, 9860123 (2021).
18. V. E. Kagan, G. Mao, F. Qu, J. P. F. Angeli, S. Doll, C. S. Croix, H. H. Dar, B. Liu, V. A. Tyurin, V. B. Ritov, A. A. Kapralov, A. A. Amoscato, J. Jiang, T. Anthonymuthu, D. Mohammadyani, Q. Yang, B. Proneth, J. Klein-Seetharaman, S. Watkins, I. Bahar, J. Greenberger, R. K. Mallampalli, B. R. Stockwell, Y. Y. Tyurina, M. Conrad, H. Bayır, Oxidized arachidonic and adrenic PEs navigate cells to ferroptosis. *Nat. Chem. Biol.* **13**, 81–90 (2017).
19. X. Ma, L. Xiao, L. Liu, L. Ye, P. Su, E. Bi, Q. Wang, M. Yang, J. Qian, Q. Yi, CD36-mediated ferroptosis dampens intratumoral $CD8^+$ Tcell effector function and impairs their antitumor ability. *Cell Metab.* **33**, 1001–1012.e5 (2021).
20. R. W. Mahley, K. H. Weisgraber, Y. Huang, Apolipoprotein E: Structure determines function, from atherosclerosis to Alzheimer's disease to AIDS. *J. Lipid Res.* **50**, S183–S188 (2009).
21. N. Pencheva, H. Tran, C. Buss, D. Huh, M. Drobnjak, K. Busam, S. F. Tavazoie, Convergent multi-miRNA targeting of ApoE drives LRP1/LRP8-dependent melanoma metastasis and angiogenesis. *Cell* **151**, 1068–1082 (2012).
22. N. Pencheva, C. G. Buss, J. Posada, T. Merghoub, S. F. Tavazoie, Broad-spectrum therapeutic suppression of metastatic melanoma through nuclear hormone receptor activation. *Cell* **156**, 986–1001 (2014).
23. K. S. Hoek, N. C. Schlegel, O. M. Eichhoff, D. S. Widmer, C. Praetorius, S. O. Einarsson, S. Valgeirsdottir, K. Bergsteinsdottir, A. Schepsky, R. Dummer, E. Steingrimsson, Novel MITF targets identified using a two-step DNA microarray strategy. *Pigment Cell Melanoma Res.* **21**, 665–676 (2008).
24. P. S. Hauser, V. Narayanaswami, R. O. Ryan, Apolipoprotein E: From lipid transport to neurobiology. *Prog. Lipid Res.* **50**, 62–74 (2011).
25. E. Zvintzou, G. Kekou, E. Xepapadaki, K. E. Kypreos, P. C. Giannopoulou, Functional interaction between apolipoproteins A2 and E in the triglyceride rich lipoprotein metabolism: Is LDLR involved? *Atherosclerosis* **331**, e123 (2021).
26. J. B. Park, C. S. Lee, J.-H. Jang, J. Ghim, Y.-J. Kim, S. You, D. Hwang, P.-G. Suh, S. H. Ryu, Phospholipase signalling networks in cancer. *Nat. Rev. Cancer* **12**, 782–792 (2012).
27. A. M. Vasquez, V. D. Mouchlis, E. A. Dennis, Review of four major distinct types of human phospholipase A2. *Adv. Biol. Regul.* **67**, 212–218 (2018).
28. D. Chen, B. Chu, X. Yang, Z. Liu, Y. Jin, N. Kon, R. Rabadan, X. Jiang, B. R. Stockwell, W. Gu, iPLA2β-mediated lipid detoxification controls p53-driven ferroptosis independent of GPX4. *Nat. Commun.* **12**, 3644 (2021).
29. W.-Y. Sun, V. A. Tyurin, K. Mikulska-Ruminska, I. H. Shrivastava, T. S. Anthonymuthu, Y.-J. Zhai, M.-H. Pan, H.-B. Gong, D.-H. Lu, J. Sun, W.-J. Duan, S. Korolev, A. Y. Abramov, P. R. Angelova, I. Miller, O. Beharier, G.-W. Mao, H. H. Dar, A. A. Kapralov, A. A. Amoscato, T. G. Hastings, T. J. Greenamyre, C. T. Chu, Y. Sadovsky, I. Bahar, H. Bayır, Y. Y. Tyurina, R.-R. He, V. E. Kagan, Phospholipase $iPLA_2\beta$ averts ferroptosis by eliminating a redox lipid death signal. *Nat. Chem. Biol.* **17**, 465–476 (2021).
30. O. Beharier, V. A. Tyurin, J. P. Goff, J. Guerrero-Santoro, K. Kajiwara, T. Chu, Y. Y. Tyurina, C. M. S. Croix, C. T. Wallace, S. Parry, W. T. Parks, V. E. Kagan, Y. Sadovsky, PLA2G6 guards placental trophoblasts against ferroptotic injury. *Proc. Natl. Acad. Sci. U.S.A.* **117**, 27319–27328 (2020).
31. Q.-Z. Tuo, Y. Liu, Z. Xiang, H.-F. Yan, T. Zou, Y. Shu, X.-L. Ding, J.-J. Zou, S. Xu, F. Tang, Y.-Q. Gong, X.-L. Li, Y.-J. Guo, Z.-Y. Zheng, A.-P. Deng, Z.-Z. Yang, W.-J. Li, S.-T. Zhang, S. Ayton, A. I. Bush, H. Xu, L. Dai, B. Dong, P. Lei, Thrombin induces ACSL4-dependent ferroptosis during cerebral ischemia/reperfusion. *Signal Transduct. Target. Ther.* **7**, 59 (2022).
32. W. Zheng, Q. Lin, M. A. Issah, Z. Liao, J. Shen, Identification of PLA2G7 as a novel biomarker of diffuse large B cell lymphoma. *BMC Cancer* **21**, 927 (2021).
33. Y.-J. Wang, S.-B. Chang, C.-Y. Wang, H.-T. Huang, S.-F. Tzeng, The selective lipoprotein-associated phospholipase A2 inhibitor darapladib triggers irreversible actions on glioma cell apoptosis and mitochondrial dysfunction. *Toxicol. Appl. Pharmacol.* **402**, 115133 (2020).
34. M. A. Gijón, C. C. Leslie, Regulation of arachidonic acid release and cytosolic phospholipase A2 activation. *J. Leukoc. Biol.* **65**, 330–336 (1999).
35. O. Rådmark, O. Werz, D. Steinhilber, B. Samuelsson, 5-Lipoxygenase: Regulation of expression and enzyme activity. *Trends Biochem. Sci.* **32**, 332–341 (2007).
36. L. Jiang, J. Zhong, X. Dou, C. Cheng, Z. Huang, X. Sun, Effects of ApoE on intracellular calcium levels and apoptosis of neurons after mechanical injury. *Neuroscience* **301**, 375–383 (2015).
37. J. D. Clark, L. L. Lin, R. W. Kriz, C. S. Ramesha, L. A. Sultzman, A. Y. Lin, N. Milona, J. L. Knopf, A novel arachidonic acid-selective cytosolic PLA_2 contains a Ca^{2+}-dependent translocation domain with homology to PKC and GAP. *Cell* **65**, 1043–1051 (1991).
38. Y. Jin, Y. W. Chung, M. K. Jung, J. H. Lee, K. Y. Ko, J. K. Jang, M. Ham, H. Kang, C. G. Pack, H. Mihara, I. Y. Kim, Apolipoprotein E-mediated regulation of selenoprotein P transportation via exosomes. *Cell. Mol. Life Sci.* **77**, 2367–2386 (2020).
39. N. Kitabayashi, S. Nakao, Y. Mita, K. Arisawa, T. Hoshi, T. Toyama, K.-A. Ishii, T. Takamura, N. Noguchi, Y. Saito, Role of selenoprotein P expression in the function of pancreatic β cells: Prevention of ferroptosis-like cell death and stress-induced nascent granule degradation. *Free Radic. Biol. Med.* **183**, 89–103 (2022).
40. Q. Ma, Role of nrf2 in oxidative stress and toxicity. *Annu. Rev. Pharmacol. Toxicol.* **53**, 401–426 (2013).
41. K.-A. Jung, B.-H. Choi, C.-W. Nam, M. Song, S.-T. Kim, J. Y. Lee, M.-K. Kwak, Identification of aldo-keto reductases as NRF2-target marker genes in human cells. *Toxicol. Lett.* **218**, 39–49 (2013).
42. X. Yu, Y. Wang, J. Tan, Y. Li, P. Yang, X. Liu, J. Lai, Y. Zhang, L. Cai, Y. Gu, L. Xu, Y. Li, Inhibition of NRF2 enhances the acute myeloid leukemia cell death induced by venetoclax via the ferroptosis pathway. *Cell Death Discov.* **10**, 35 (2024).
43. L. Feng, K. Zhao, L. Sun, X. Yin, J. Zhang, C. Liu, B. Li, SLC7A11 regulated by NRF2 modulates esophageal squamous cell carcinoma radiosensitivity by inhibiting ferroptosis. *J. Transl. Med.* **19**, 367 (2021).
44. H. Dong, Y. Xia, S. Jin, C. Xue, Y. Wang, R. Hu, H. Jiang, Nrf2 attenuates ferroptosis-mediated IIR-ALI by modulating TERT and SLC7A11. *Cell Death Dis.* **12**, 1027 (2021).
45. M. Dodson, R. Castro-Portuguez, D. D. Zhang, NRF2 plays a critical role in mitigating lipid peroxidation and ferroptosis. *Redox Biol.* **23**, 101107 (2019).
46. B. N. Ostendorf, J. Bilanovic, N. Adaku, K. N. Tafreshian, B. Tavora, R. D. Vaughan, S. F. Tavazoie, Common germline variants of the human *APOE* gene modulate melanoma progression and survival. *Nat. Med.* **26**, 1048–1053 (2020).
47. Y. He, J. Chen, Y. Ma, H. Chen, Apolipoproteins: New players in cancers. *Front. Pharmacol.* **13**, 1051280 (2022).

48. Y. Huang, R. W. Mahley, Apolipoprotein E: Structure and function in lipid metabolism, neurobiology, and Alzheimer's diseases. *Neurobiol. Dis.* **72**, 3–12 (2014).
49. P. Prasinou, I. Dafnis, G. Giacometti, C. Ferreri, A. Chroni, C. Chatgilialoglu, Fatty acid-based lipidomics and membrane remodeling induced by apoE3 and apoE4 in human neuroblastoma cells. *Biochim. Biophys. Acta Biomembr.* **1859**, 1967–1973 (2017).
50. H.-S. Hoe, D. C. Harris, G. W. Rebeck, Multiple pathways of apolipoprotein E signaling in primary neurons. *J. Neurochem.* **93**, 145–155 (2005).
51. Y. Yamazaki, N. Zhao, T. R. Caulfield, C.-C. Liu, G. Bu, Apolipoprotein E and Alzheimer disease: Pathobiology and targeting strategies. *Nat. Rev. Neurol.* **15**, 501–518 (2019).
52. Y.-W. A. Huang, B. Zhou, A. M. Nabet, M. Wernig, T. C. Südhof, Differential signaling mediated by Apoe2, Apoe3, and Apoe4 in human neurons parallels Alzheimer's disease risk. *J. Neurosci.* **39**, 7408–7427 (2019).
53. L. Zhou, H. Y. Choi, W.-P. Li, F. Xu, J. Herz, LRP1 controls cPLA$_2$ phosphorylation, ABCA1 expression and cellular cholesterol export. *PLOS ONE* **4**, e6853 (2009).
54. Z. Li, L. Ferguson, K. K. Deol, M. A. Roberts, L. Magtanong, J. M. Hendricks, G. A. Mousa, S. Kilinc, K. Schaefer, J. A. Wells, M. C. Bassik, A. Goga, S. J. Dixon, N. T. Ingolia, J. A. Olzmann, Ribosome stalling during selenoprotein translation exposes a ferroptosis vulnerability. *Nat. Chem. Biol.* **18**, 751–761 (2022).
55. M. A. Greenough, D. J. R. Lane, R. Balez, H. T. D. Anastacio, Z. Zeng, K. Ganio, C. A. McDevitt, K. Acevedo, A. A. Belaidi, J. Koistinaho, L. Ooi, S. Ayton, A. I. Bush, Selective ferroptosis vulnerability due to familial Alzheimer's disease presenilin mutations. *Cell Death Differ.* **29**, 2123–2136 (2022).
56. H. Alborzinia, Z. Chen, U. Yildiz, F. P. Freitas, F. C. E. Vogel, J. P. Varga, J. Batani, C. Bartenhagen, W. Schmitz, G. Büchel, B. Michalke, J. Zheng, S. Meierjohann, E. Girardi, E. Espinet, A. F. Flórez, A. F. D. Santos, N. Aroua, T. Cheytan, J. Haenlin, L. Schlicker, T. N. X. da, Silva, A. Przybylla, P. Zeisberger, G. Superti-Furga, M. Eilers, M. Conrad, M. Fabiano, U. Schweizer, M. Fischer, A. Schulze, A. Trumpp, J. P. F. Angeli, LRP8-mediated selenocysteine uptake is a targetable vulnerability in MYCN-amplified neuroblastoma. *EMBO Mol. Med.* **15**, e18014 (2023).
57. N. Adaku, B. N. Ostendorf, W. Mei, S. F. Tavazoie, Apolipoprotein E2 stimulates protein synthesis and promotes melanoma progression and metastasis. *Cancer Res.* **83**, 3013–3025 (2023).
58. M. Miyata, J. D. Smith, Apolipoprotein E allele-specific antioxidant activity and effects on cytotoxicity by oxidative insults and β-amyloid peptides. *Nat. Genet.* **14**, 55–61 (1996).
59. A. A. Belaidi, S. Masaldan, A. Southon, P. Kalinowski, K. Acevedo, A. T. Appukuttan, S. Portbury, P. Lei, P. Agarwal, S. E. Leurgans, J. Schneider, M. Conrad, A. I. Bush, S. Ayton, Apolipoprotein E potently inhibits ferroptosis by blocking ferritinophagy. *Mol. Psychiatry* **29**, 211–220 (2022).
60. X. Ma, X. Dong, Y. Xu, N. Ma, M. Wei, X. Xie, Y. Lu, W. Cao, G. Lu, W. Li, Identification of AP-1 as a critical regulator of glutathione peroxidase 4 (GPX4) transcriptional suppression and acinar cell ferroptosis in acute pancreatitis. *Antioxidants* **12**, 100 (2022).
61. S. Tang, J. Liu, F. Li, Y. Yan, X. Long, Y. Fu, AP-1 inhibitor induces ferroptosis via the PI3K/AKT pathway in multiple myeloma cells. *Heliyon* **10**, e34397 (2024).
62. Z. Wang, X. Zhang, X. Tian, Y. Yang, L. Ma, J. Wang, Y. Yu, CREB stimulates GPX4 transcription to inhibit ferroptosis in lung adenocarcinoma. *Oncol. Rep.* **45**, 88 (2021).
63. L. Cao, Y. Wang, J. Liu, X. Bai, X. Chi, Long non-coding RNA TPT1-AS1 inhibits ferroptosis in ovarian cancer by regulating GPX4 via CREB1 regulation. *Am. J. Reprod. Immunol.* **92**, e13864 (2024).
64. S. Zhu, Q. Zhang, X. Sun, H. J. Zeh, M. T. Lotze, R. Kang, D. Tang, HSPA5 regulates ferroptotic cell death in cancer cells. *Cancer Res.* **77**, 2064–2077 (2017).
65. M. Wang, J. Tang, S. Zhang, K. Pang, Y. Zhao, N. Liu, J. Huang, J. Kang, S. Dong, H. Li, Z. Tian, B. Duan, F. Lu, W. Zhang, Exogenous H_2S initiating Nrf2/GPx4/GSH pathway through promoting Syvn1-Keap1 interaction in diabetic hearts. *Cell Death Discov.* **9**, 394 (2023).
66. T. Zhao, Z. Yu, L. Zhou, X. Wang, Y. Hui, L. Mao, X. Fan, B. Wang, X. Zhao, C. Sun, Regulating Nrf2-GPx4 axis by bicyclol can prevent ferroptosis in carbon tetrachloride-induced acute liver injury in mice. *Cell Death Discov.* **8**, 380 (2022).
67. I. Arozarena, C. Wellbrock, Phenotype plasticity as enabler of melanoma progression and therapy resistance. *Nat. Rev. Cancer* **19**, 377–391 (2019).
68. X. Li, J. Zhang, D. Li, C. He, K. He, T. Xue, L. Wan, C. Zhang, Q. Liu, Astrocytic ApoE reprograms neuronal cholesterol metabolism and histone-acetylation-mediated memory. *Neuron* **109**, 957–970.e8 (2021).
69. A. Sen, T. J. Nelson, D. L. Alkon, Apoe4 and aβ oligomers reduce BDNF expression via HDAC nuclear translocation. *J. Neurosci.* **35**, 7538–7551 (2015).
70. O. Meçe, D. Houbaert, M.-L. Sassano, T. Durré, H. Maes, M. Schaaf, S. More, M. Ganne, M. García-Caballero, M. Borri, J. Verhoeven, M. Agrawal, K. Jacobs, G. Bergers, S. Blacher, B. Ghesquière, M. Dewerchin, J. V. Swinnen, S. Vinckier, M. S. Soengas, P. Carmeliet, A. Noël, P. Agostinis, Lipid droplet degradation by autophagy connects mitochondria metabolism to Prox1-driven expression of lymphatic genes and lymphangiogenesis. *Nat. Commun.* **13**, 2760 (2022).
71. J. Chen, Q. Li, J. Wang, Topology of human apolipoprotein E3 uniquely regulates its diverse biological functions. *Proc. Natl. Acad. Sci. U.S.A.* **108**, 14813–14818 (2011).

Acknowledgments: We thank K. Rillaerts and J. Dehairs for expert technical support and A. Talebi for sharing tools and advice. We acknowledge the VIB Bio Imaging Core for support and assistance. We also acknowledge the laboratory of B. De Strooper for proving the APOE-deficient mice. We acknowledge TRACE, the KULeuven PDX facility. Figures were created with BioRender.com . **Funding:** This work was supported by grants from the Flemish Research Foundation (FWO-Vlaanderen, G0A3320N), the Stichting tegen Kanker (F/2022/2037), the KU Leuven C14/21/095 InterAction consortium, the EOS DECODE consortium no. 30837538, the EOS MetaNiche consortium no. 40007532, and the iBOF/21/053 ATLANTIS network to P.A. S.M. was a fellow of the Marie Curie TRAINERS consortium. F.R. received doctoral fellowship and J.B. a postdoctoral fellowship from the Flemish Research Foundation (FWO-Vlaanderen). B.R.S. is supported by the NCI/NIH (R35CA209896). F.B. is supported by the Flemish Research Foundation (FWO-Vlaanderen; I005920N and 1801821N). **Author contributions:** Conceptualization: P.A., P.K., J.V.S., S.M., J.C.M., and B.R.S. Methodology: J.V., P.K., J.V.S., D.W., T.K., F.B., J.B., T.V., and S.M. Investigation: D.N., J.V., E.V., P.K., M.G., F.R., F.B., J.B., X.S., T.V., and S.M. Visualization: P.A., D.W., T.K., and S.M. Supervision: P.A., D.L., J.C.M., F.B., and A.S. Writing—original draft: P.A. and S.M. Writing—review and editing: P.A., O.B., J.B., J.V.S., S.N., and S.M. Resources: O.B., D.L., P.K., J.C.M., F.B., and J.V.S. Project administration: P.A., O.B., D.L., F.B., and A.S. Funding acquisition: P.A. and D.L. Formal analysis: T.V., D.W., T.K., S.N., F.B., X.S., and S.M. Data curation: P.A., D.L., T.K., F.B., and S.M. Validation: P.A., T.V., S.N., F.B., X.S., and S.M. Software: P.K., T.V., T.K., D.W., S.N., and S.M. All authors discussed the results and commented on the manuscript. **Competing interests:** B.R.S. is an inventor on patents and patent applications involving small-molecule drug discovery and ferroptosis, has equity in and serves as a consultant to Exarta Therapeutics and ProJenX Inc., holds equity in Sonata Therapeutics, and serves as a consultant to Weatherwax Biotechnologies Corporation and Akin Gump Strauss Hauer & Feld LLP. The other authors declare that they have no competing interests. **Data and materials availability:** All data needed to evaluate the conclusions in the paper are present in the paper and/or the Supplementary Materials. The WM852 cell line can be provided by M. Herlyn pending scientific review and a completed material transfer agreement. Requests for the WM852 cell line should be submitted to: jkohn@wistar.org.

Submitted 3 April 2024
Accepted 11 September 2024
Published 16 October 2024
10.1126/sciadv.adp6164